Mon. Not. R. Astron. Soc. **000**, 1–?? (2008) Printed 22 October 2008 (MN LaTeX style file v2.2)

arXiv:0810.3660v1 [astro-ph] 21 Oct 2008

Globular Cluster Systems in Nearby Dwarf Galaxies: I. HST/ACS Observations and Dynamical Properties of Globular Clusters at Low Environmental Density

Iskren Y. Georgiev[1,2⋆], Thomas H. Puzia[3], Michael Hilker[4], and Paul Goudfrooij[2]

[1] *Argelander Institut für Astronomie der Universität Bonn, Auf dem Hügel 71, D-53121 Bonn, Germany*
[2] *Space Telescope Science Institute, 3700 San Martin Drive, Baltimore, MD 21218, USA*
[3] *Herzberg Institute for Astrophysics, 5071 Saanich Road, Victoria, BC V9E 2E7, Canada*
[4] *European Southern Observatory, D-85748 Garching bei München, Germany*

October 2008

ABSTRACT

We investigate the old globular cluster (GC) population of 68 faint ($M_V > -16$ mag) dwarf galaxies located in the halo regions of nearby ($\lesssim 12$ Mpc) loose galaxy groups and in the field environment based on archival HST/ACS images in F606W and F814W filters. The combined color distribution of 175 GC candidates peaks at $(V-I) = 0.96 \pm 0.07$ mag and the GC luminosity function turnover for the entire sample is found at $M_{V,\mathrm{TO}} = -7.6 \pm 0.11$ mag, similar to the old metal-poor LMC GC population. Our data reveal a tentative trend of $M_{V,\mathrm{TO}}$ becoming fainter from late-type to early-type galaxies. The luminosity and color distributions of GCs in dIrrs shows a lack of faint blue GCs. Our analysis reveals that this might reflect a relatively younger GC system than typically found in luminous early-type galaxies. If verified by spectroscopy this would suggest a later formation epoch of the first metal-poor star clusters in dwarf galaxies. We find several bright (massive) GCs which reside in the nuclear regions of their host galaxies. These nuclear clusters have similar luminosities and structural parameters as the peculiar Galactic clusters suspected of being the remnant nuclei of accreted dwarf galaxies, such as M54 and ωCen. Except for these nuclear clusters, the distribution of GCs in dIrrs in the half-light radius vs. cluster mass plane is very similar to that of Galactic young halo clusters, which suggests comparable formation and dynamical evolution histories. A comparison with theoretical models of cluster disruption indicates that GCs in low-mass galaxies evolve dynamically as self-gravitating systems in a benign tidal environment.

Key words: galaxies : dwarf – galaxies : irregular – galaxies : star clusters

1 INTRODUCTION

Globular clusters (GCs) are observed in vast numbers in massive early-type galaxies (e.g. Harris et al. 2006) and the integrated-light properties of GCs were extensively studied in the last decade (e.g. Kissler-Patig et al. 1997; Hilker et al. 1999; Kundu & Whitmore 2001a,b; Larsen et al. 2001; Goudfrooij et al. 2003; Puzia et al. 2002, 2004; Harris et al. 2006; Jordán et al. 2005, 2007; Peng et al. 2006, 2008) with the aim to understand how such populous GC systems were assembled. These studies revealed the discovery of *i*) the bimodal metallicity/color distribution of GCs (e.g. Ashman & Zepf 1992; Gebhardt & Kissler-Patig 1999; Puzia et al. 1999; Kundu & Whitmore 2001a, and references therein) and *ii*) the presence of young and intermediate-age globular clusters in merging, starburst, and quiescent galaxies (e.g. Whitmore & Schweizer 1995; Goudfrooij et al. 2001, 2007; Puzia et al. 2002; Schweizer 2002).

From the point of view of GC system assembly, multiple scenarios for galaxy formation have been presented to explain these findings. The first scenario is the *hierarchical* build-up of massive galaxies from pregalactic dwarf-sized gas fragments (Searle & Zinn 1978) in which the metal-poor GCs form *in situ* while the metal-rich GCs originate from a second major star formation event (Forbes et al. 1997) or infalling gaseous fragments, the so-called mini-mergers at high redshifts (Beasley et al. 2002). The *dissipative merger* scenario (e.g. Schweizer 1987; Ashman & Zepf 1992; Bekki et al. 2002) assumes that the metal-poor GCs were formed early in "Searle-Zinn" fragments while metal-rich

---

⋆ E-mail: iskren@astro.uni-bonn.de

(and younger) GCs formed during major merger events of galaxies with comparable masses (Spiral–Spiral, Elliptical–Spiral, etc.). The *dissipationless merging and accretion* scenario incorporates the classical monolithic galaxy collapse in which the galaxies and their GCs were formed after which the dwarf galaxies and their GCs were accreted by giant galaxies (Zinn 1993; Côté et al. 1998, 2002; Hilker et al. 1999; Lee et al. 2007). For detailed discussions on the GC systems formation and assembly scenarios and properties of GCs in various galaxy types we refer the reader to Kissler-Patig (2000); van den Bergh (2000); Harris (2001, 2003); Brodie & Strader (2006).

Dwarf galaxies play an important role in assessing the likelihoods of the formation scenarios mentioned above. The prediction of the hierarchical growth of massive galaxies through merging of many dwarf-sized fragments at early times is backed by the steepening of the faint-end slope of the galaxy luminosity function with redshift (e.g. Ryan et al. 2007; Khochfar et al. 2007). In addition, the observed fraction of low-mass irregular galaxies increases with redshift (e.g. Conselice et al. 2008), and Hubble Ultra Deep field studies show that dwarf-sized irregular galaxies dominate at $z \gtrsim 6$ (e.g. Stiavelli et al. 2004). Hence, the oldest stellar populations in nearby dIrr galaxies may thus represent the probable *surviving* early building blocks of massive galaxies.

Evidence for accretion events of dwarf galaxies and their dissolution in the Galactic potential is manifested by a few tidal stellar streams observed in the Milky Way, M31, and other nearby galaxies (e.g. Ibata et al. 2001; Grillmair 2006; Liu et al. 2006; Martinez-Delgado et al. 2008, and references therein). A well-known example of a recent accretion event is the Sagittarius dwarf galaxy, which is currently being added to the Milky Way halo together with its globular clusters (e.g., Ibata et al. 1994). Many more such minor accretion/merger events of dwarf sized galaxies are expected during the hierarchical evolution of giant galaxies. The Pipino et al. (2007) galaxy evolution and GC formation model, in which a low number of blue (metal-poor) GCs in massive galaxies are predicted to form in the initial (”monolithic”) collapse, contrasts with observations and suggests that subsequent accretion of such metal-poor GCs from low-mass dwarfs is required (Côté et al. 1998, 2002). However, the observed large ratio between metal-poor GCs and metal-poor field halo stars in massive galaxies (Harris 2001; Harris & Harris 2002) implies that, if such dwarfs were later accreted, they must have had large GC specific frequencies S_N[1] in order to keep the GC-to-field-star ratio high. This is in line with the high specific frequencies observed in low-mass early and late-type dwarfs in galaxy clusters (Durrell et al. 1996; Miller et al. 1998; Seth et al. 2004; Miller & Lotz 2007; Georgiev et al. 2006; Peng et al. 2008) and in group/field environments (Olsen et al. 2004; Sharina et al. 2005; Georgiev et al. 2008; Puzia & Sharina 2008).

In this series of papers we will present results from an analysis of old GCs in 68 dwarf galaxies in nearby loose groups and in the field. The current paper is organized as follows. In §2 we describe the target sample, discuss the completeness and contamination, and define the globular cluster candidate selection. In §3 the colors, luminosities, and structural parameters are compared with old Local Group GCs, and a discussion of the dynamical state of the globular clusters in our sample dwarfs. Section §4 summarizes our results.

Table 1. Summary of target sample. The table shows the number of morphological galaxy types observed in each program and the total sample. The bottom row shows the number of galaxies in which we found globular cluster candidates.

Program ID	dIrr	dE	dSph	Sm
SNAP 9771	26	2	4	2
GO-10235	10	1	1	3
GO-10210	19	–	–	–
$\Sigma_{\rm all}$	55	3	5	5
$\Sigma_{\rm w/GC}$	30	2	2	4

2 DATA

2.1 Observations

The current study is based on HST/ACS archival data from programs SNAP-9771 and GO-10235, conducted in HST cycles 12 and 13, respectively (PI: I. Karachentsev), and archival HST/ACS data (GO-10210, PI: B. Tully) that were described in Georgiev et al. (2008). A summary of the various datasets is provided in Table 1.

Non-dithered 2 × 600 s F606W and 2 × 450 s F814W exposures for each galaxy were designed to reach the Tip of the Red Giant Branch (TRGB) at $M_I = -4.05$ or $M_V = -2.75$ to -1.45 mag in the range [Z/H] $= -2.2$ to -0.7 dex (Da Costa & Armandroff 1990) and provide TRGB distances to the sample dwarf galaxies as published in Karachentsev et al. (2006, 2007). All galaxies reside in the isolated outskirts of nearby ($\leqslant 6$ Mpc) galaxy groups (Sculptor, Maffei 1& 2, IC 342, M 81, CVn I cloud) with the exception of 3 very isolated dwarfs within 12 Mpc.

The program SNAP-9771 observed 34 low-mass galaxies, of which 26 are dIrrs, 2 dEs, 4 dSphs and 2 late-type spiral dwarf galaxies. The program GO-10235 contains 15 targets of which 10 are dIrrs, 1 dE, 1 dSph and 3 late-type spirals. All galaxies in our final sample have published TRGB distance measurements (Karachentsev et al. 2006, 2007). A summary of their general properties is given in Table 2. In column (1) the galaxy IDs are listed, and in columns (2) and (3) their coordinates; columns (4) and (5) contain the morphological classifications from LEDA[2] and NED[3], (6) and (7) list the distances and distance moduli, in (8) is the foreground galactic extinction (E_{B-V}), (9) and (10) give the absolute magnitudes and colors (measured in this work, see Section 3.1), and in column (11) we provide their HI mass (obtained from LEDA).

The additional archival HST/ACS data consists of 19 Magellanic-type dIrr galaxies residing in nearby ($2-8$ Mpc) associations composed mainly of dwarfs with similar luminosities as the target galaxies, with the only exception that the previous sample was composed of dwarfs located in isolated associations of only few dwarfs (Tully et al. 2006), while the dwarfs in our new dataset are in the halo regions of groups which contain massive dominant galaxies such as M 83 and Cen A (Karachentsev et al. 2006, 2007, see Table 2). The HST/ACS F606W and F814W imaging of the previous data was also designed to reach the tip of the red giant branch (TRGB) and measure TRGB distances (Tully et al. 2006).

---

[1] S_N is the number of GCs per unit galaxy luminosity (Harris & van den Bergh 1981).

[2] http://leda.univ-lyon1.fr/

[3] http://nedwww.ipac.caltech.edu/

In total, our sample consists of 55 dIrrs, 3 dEs, 5 dSphs, and 5 Sm galaxies in the field environment. All dwarfs have apparent diameters smaller than the HST/ACS field of view which provided us with a good sampling of their GCSs.

2.2 Data Reduction and Photometry

Image processing and photometry was performed in a manner identical to that in our previous study described in Georgiev et al. (2008). In the following we briefly summarize the basic steps. We retrieved archival HST/ACS images in F606W and F814W filters which were processed with the ACS reduction pipeline and the MULTIDRIZZLE routine (Koekemoer et al. 2002). To improve the object detection and photometry we modeled and subtracted the underlying galaxy light using a circular aperture median kernel of 41 pixel radius. This choice of filter radius at 3 Mpc (the closest galaxy) corresponds to ~ 30 pc, which is ten times the typical GC $r_{\rm h}$. This is large enough that after median galaxy light subtraction, the structure of the GC candidates will be preserved.

Object detection (4σ above the background) and initial aperture photometry (in 2,3,5 and 10 pixel radius) was performed with the IRAF[4] DAOPHOT/DAOFIND and PHOT routines. Conversion from instrumental magnitudes to the STMAG system and aperture corrections from 10 pixel to infinity were performed using the ACS photometric calibration prescription by Sirianni et al. (2005).

2.3 GC Candidate Selection

The first step in our GC candidate[5] selection was based on the expected colors for old (> 4 Gyr) Simple Stellar Population (SSP) models (Anders & Fritze-v. Alvensleben 2003; Bruzual & Charlot 2003) and typical colors of old Galactic GCs, namely objects in the color range $-0.4 \leqslant$(F606W-F814W)$\leqslant 0.2$ (corresponding to $0.7 < V-I < 1.5$). Second, we have imposed a faint magnitude cut-off at the TRGB ($M_V = -2.5$, $M_I = -4.05$; Da Costa & Armandroff 1990; Lee et al. 1993) converted to apparent magnitudes according to the distance to each galaxy as derived by Tully et al. (2006) and Karachentsev et al. (2006, 2007). This is ∼5 mag fainter than the typical GC luminosity function turnover magnitude for metal-poor Galactic globular clusters at $M_{V,\,\rm TO} = -7.66 \pm 0.1$ mag (e.g. Di Criscienzo et al. 2006).

Due to the deep ACS imaging and its high spatial resolution (1 ACS pixel being equivalent to 1.2 pc at a mean distance to our sample dIrrs of 5 Mpc), a typical Local Group GC with half-light radius of $r_{\rm h} = 3$ pc is resolved. We used the IMEXAM task within IRAF to confine the initial GC selection to round objects ($\mathrm{FWHM}_{F606W} \simeq \mathrm{FWHM}_{F814W}$) with an IMEXAM ellipticity $\epsilon \leqslant 0.15$ within a fixed $r = 5$ pix aperture radius and a Moffat index $\beta = 2.5$, typical for stellar profiles. As we showed in Georgiev et al. (2008), the upper IMEXAM ϵ limit allows selection of GCs with true ellipticity up to $\epsilon < 0.4$. The final ellipticities and half-light radii ($\epsilon,\ r_{\rm h}$) were measured with ISHAPE (see Sect. 2.4).

The last GC selection step is to measure the differences between the aperture photometry determined using 2, 3, and 5 pixel radii. These $\mathrm{m}_2{-}\mathrm{m}_3$ vs. $\mathrm{m}_2{-}\mathrm{m}_5$ concentration indices separate well the unresolved foreground stars from extended GCs and the majority of the contaminating background galaxies during the automated GC selection.

We have detected 57 old GC candidates in 17 dIrrs, 6 GCs in 2 dSph, 25 GCs in 2 dEs and 25 GCs in 4 Sm dwarfs. Therefore, in combination with the 60 GCs from Georgiev et al. (2008) we have in total 117 GCs in 30 dIrrs. The total number of GCs in our sample contains: 119 in dIrrs, of which 64 are bGCs and 42 rGCs; in dEs/dSphs the number of GCs sums up to 31 with 21 bGCs and 10 rGCs; the low-mass late-type spirals contain 26 GCs in total, with 13 bGCs and 11 rGCs. The properties of all GC candidates are listed in Table 3 with the cluster ID and its coordiantes in columns (2) and (3); cluster absolute magnitude and foreground dereddened color $(V-I)_0$ in (3) and (4); cluster half-light radius and ellipticity ($r_{\rm h}$, ϵ, respectively) in (5) and (6) as derived in Sect. 2.4 and their projected distance from the galactic center ($r_{\rm proj}$) and the normalized to the effective galaxy radius projected distance ($r_{\rm proj}/r_{\rm eff}$) in (7) and (8), respectively. Finding charts of all GCs are presented in the Appendix in Figure 9.

The final GC photometry was derived from curve of growth analysis for each individual object from images iteratively cleaned from contaminating sources within the photometric apertures. A detailed description of this iterative procedure is provided in Georgiev et al. (2008) and will not be repeated here.

Conversion from STMAG to Johnson/Cousins was performed using the transformation and dereddening coefficients (for a G2 star) provided in Sirianni et al. (2005). The Galactic foreground reddening E_{B-V} toward each galaxy was obtained from the Schlegel et al. (1998) maps.

2.4 Structural parameters

To derive the GC structural parameters (half-light radius, $r_{\rm h}$, and ellipticities, ϵ) we have used the ISHAPE algorithm (Larsen 1999), which models the object's surface brightness profile with analytical models convolved with a subsampled point spread function (PSF). Since most clusters are marginally resolved, a very good knowledge of the ACS PSF is required to obtain reliable measurements of their sizes. Testing the influence of the PSF library, we performed a comparison between the $r_{\rm h}$ measured using TinyTim[6] model PSFs (TT-PSF) and the empirical, local PSF (lPSF), built from stars in the image of each galaxy.

---

[4] IRAF is distributed by the National Optical Astronomy Observatories, which are operated by the Association of Universities for Research in Astronomy, Inc., under cooperative agreement with the National Science Foundation.

[5] In the following we refer to globular cluster candidates as GCs.

The ten times sub-sampled TT-PSF was convolved with the charge diffusion kernel. The position-dependent lPSFs was built from images typically having more than 20 isolated stars across the ACS field. For a few galaxies with a very low point-source density, we use the lPSF library from ESO 223-09, which has the maximum number of good PSF stars of all galaxies in our sample (69). Both PSF types were used with ISHAPE to model the cluster profiles for the all available King model concentration parameters ($C = r_{\rm tidal}/r_{\rm core} = 5, 15, 30, 100$). The final cluster parameters were adopted from the best χ^2 fit model for both PSFs. For the final cluster half-light radius we have adopted the geometric mean from the ISHAPE FWHMs measured along the semi-major and semi-minor axis (w_y and w_y), i.e. $r_{\rm h} = r_{{\rm h},w_y}\sqrt{w_x/w_y}$.

Figure 1 shows a comparison between the $r_{\rm h}$ derived from the best-fit TT-PSF and lPSF models. It is obvious that for every concentration parameter the $r_{\rm h,lPSF}$ values are smaller than the $r_{\rm h,TT}$ values (see Δr values in Fig. 1). This shows that the TinyTim PSFs are sharper than the empirical lPSFs which represent the actual imaging conditions (incl. charge diffusion, telescope focus breathing, drizzle effects, etc.).

In this study we are compiling data from our previous study (Georgiev et al. 2008) in which the $r_{\rm h}$ were derived from the best χ^2 TT-PSF due to the lack of enough good PSF stars for modeling the lPSF in the field of those extremely isolated dIrrs. Therefore, we convolved the GCs from that study with the local PSF derived from the image of ESO 223-09. We point out that variable telescope focus changes may introduce unknown systematics. In the bottom right panel of Fig. 1 we show the $r_{\rm h}$ derived with the TinyTim PSF versus the empirical PSF for the best χ^2 model. As can be seen, the values computed with TT-PSFs are ~ 0.4 pix larger than the corresponding sizes computed with the empirical lPSFs.

A similar difference between the empirical lPSF and the TT-PSF of ~ 0.5 pix (the $r_{\rm h,TT}$ being larger) was also previously reported in the ACS study of the Sombrero galaxy by Spitler et al. (2006) (their Fig.2), where a fixed concentration index $C = 30$ was assumed. In the following, we will use the structural parameters of GCs obtained with the empirical lPSFs.

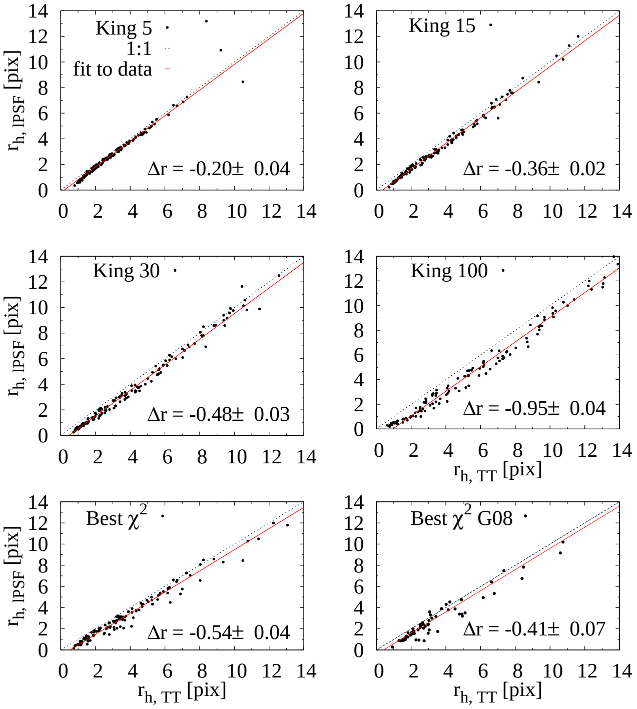

Figure 1. Comparison between $r_{\rm h}$ derived with TinyTim (TT) and empirical PSFs build from the images (lPSF). From top to bottom are shown relations for different King model concentration parameters and the best χ^2 fit models, respectively. The lower right panel shows the best χ^2 from our previous study (Georgiev et al. 2008). The solid line shows the 1:1 relation.

2.5 Completeness Tests

Artificial clusters were modeled with the MKCMPPSF and MKSYNTH routines in the BAOLAB package (Larsen 1999). The procedure includes convolution of empirical PSFs with analytic KING profiles for all concentrations (C = 5, 15, 30 and 100). For the completeness tests we chose the galaxy ESO 223-09 which has the highest surface brightness, foreground extinction ($E_{B-V} = 0.260$) and foreground star contamination in our sample (cf. Fig. 9). We point out that this is the most conservative estimate of the photometric completeness among our sample galaxies, i.e., all other sample galaxies have more complete GC samples. To sample the parameter space typical for colors and luminosities of old GCs ($t \geqslant 4$ Gyr) we generated synthetic clusters in the range $21 <$ F606W < 26 mag (STMAG) with the fainter limit matching the TRGB at the distance of ESO 223-09 (Karachentsev et al. 2007). The colors of the artificial clusters were spread over the range $-0.4 < F606W - F814W < 0.25$ ($0.5 < V - I < 1.5$) in fourteen color bins with 0.05 mag step. For each color bin 200 arificial clusters were randomly placed across the synthetic image. This step was repeated 100 times thus providing 20 000 objects per color bin or in total 280 000 artificial clusters for the completeness test for one King profile concentration. The same procedure was applied to all four concentration parameters provided within BAOLAB.

The synthetic images consist of the modeled clusters on a constant (0 ADUs) background, matching the mean background value of the original ACS images. Every synthetic image, containing 200 objects, was then added to the original ESO 223-09 image, thus preserving the image background level and noise characteristics. The final images were then subjected through the same routines for object detec-

---

[6] http://www.stsci.edu/software/tinytim/tinytim.html
The TinyTim software package takes into account the field-dependent WFC aberration, filter passband effects, charge diffusion variations, and varying pixel area due to the significant field distortion in the ACS field of view (Krist & Hook 2004).

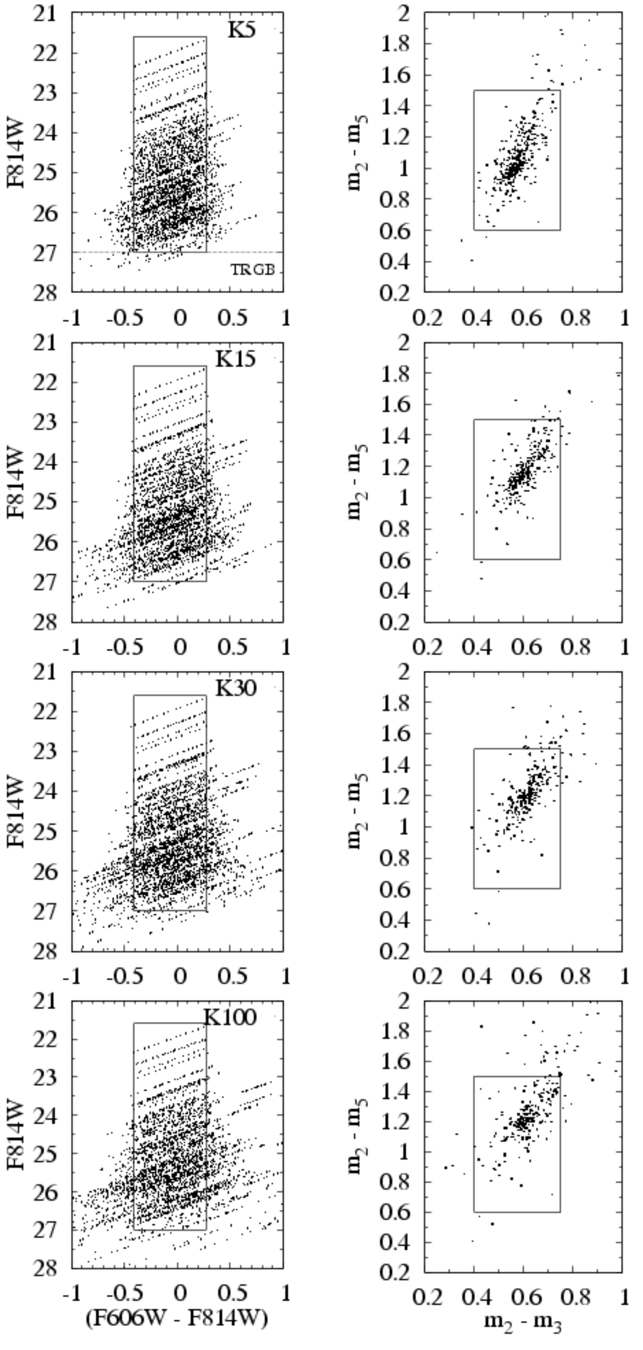

Figure 2. *Left panels:* Color-magnitude diagrams of the artificial clusters with King profile concentrations $C = 5, 15, 30$ and 100 from top to bottom, respectively. The solid line rectangle indicates the color-magnitude region used to generate artificial clusters and their subsequent selection. *Right panels:* Magnitude concentration index of the artificial clusters as defined by their 2,3 and 5 pixel aperture radius magnitudes. The rectangle defines the final cluster selection.

tion, photometry, and GC selection as the ones used to define the science sample.

In Figure 2 we show the color-magnitude diagrams (CMDs) and concentration parameter plots of the retrieved artificial clusters for the four King models. The rectangle in the left-column panels indicates the region in which the artificial clusters were modeled and later selected. After applying the color-magnitude and the IMEXAM FWHM and ϵ cuts, the final cluster selection was based on their concentration parameters as derived from the difference between their magnitudes in 2, 3 and 5 pixel aperture radius. The right-column panels of Figure 2 show the $m_2 - m_3$ vs. $m_2 - m_5$ diagrams. The objects that survived all the selection criteria were used to compute the completeness as a function of the cluster magnitude. In Figure 3 we present the completeness functions in V and I for all King models.

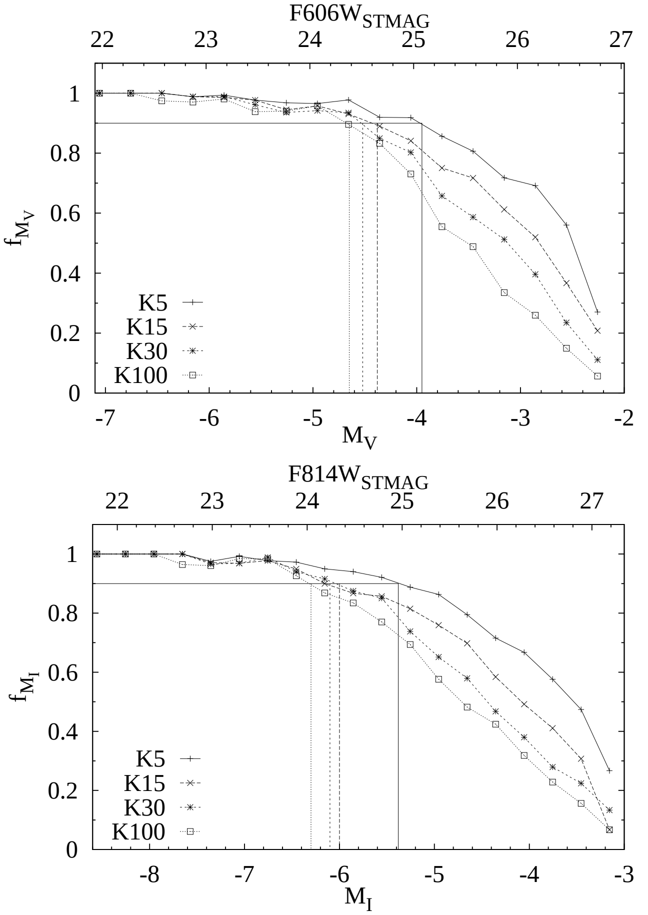

Figure 3. Completeness as a function of synthetic cluster magnitude for V and I in the top and bottom panels, respectively. To convert from instrumental STMAG to the Johnson/Cousins photometric system, we have used the transformation relations tabulated in Sirianni et al. (2005). To convert from apparent to absolute magnitudes, we have used the distance modulus of $m - M = 29.06$ mag to ESO 223-09 as derived from the TRGB measurement by Karachentsev et al. (2007).

Figure 3 shows that for the case of a galaxy with high surface brightness, strong foreground reddening and foreground star contamination (cf. Fig. 9), the 90% completness limit for extended sources is reached at $M_V \simeq -4.5$ mag. As expected, the completeness is a function of the cluster size, in the sense that more extended clusters suffer stronger incompleteness as their detection and correct magnitude measurement are easily affected by the variable galaxy background and bright foreground stars. We point out that this is the least complete case in our sample and that all other target galaxies have fainter completeness limits. For all our target galaxies we sample more than 99% of the total GCLF, in terms of luminosity and mass.

2.6 Background Contamination

Background contamination from bulges of compact galaxies at intermediate redshifts, which resemble the colors and structural appearance of GCs need to be taken into account. We have already assessed the expected contamination for the ACS field of view and objects with identical magnitude and size distributions as GCs in galaxies within 8 Mpc using the Hubble Ultra Deep Field (HUDF)[7] (Georgiev et al. 2008). The expected number of contaminating background galaxies increases significantly for $V_0 \geqslant 25$ mag ($M_V \geqslant -4$), well beyond the luminosity distribution of GCs. Nevertheless, down to this limit a contamination of up to 2 objects per field is expected.

3 ANALYSIS

3.1 Integrated Galaxy Magnitudes

Only six of the dwarf galaxies in our sample have total $V-$band magnitudes available in the literature while the majority of them only have B magnitudes. However, good knowledge of the V-band magnitudes is required to estimate their GC specific frequencies for a robust comparison with previous studies. Hence, we performed integrated-light photometry on the ACS images and derived their total magnitudes.

Bright foreground stars and background galaxies were masked out and replaced with the local background level and noise. The median smoothed image of each galaxy was used to estimate the center of the galaxy. However, for most dwarfs the derived centers were not representative of the visual center of the extended galaxy light, but rather the region with the strongest starburst. Thus, we adopted the geometric center of the isointensity contour at the 10σ level above the background as the galaxy center. Since the galaxies rarely extend beyond 1500 pixel radius, the estimate of the sky value determined from the median value measured at the image corners, is representative for the true photometric background. To measure the galaxy magnitudes we used the ELLIPSE task within IRAF. The initial values for galaxy ellipticity and position angle were taken from NED. For dwarfs without published values for those parameters, we estimated the center in interactive mode with ELLIPSE, i.e. to approximate the ellipticity and position angle of the extended light (at the 10σ isointensity contour). We have measured the total galaxy magnitudes within the ellipse with radius at the Holmberg radius ($\mu_B = 26.5$) quoted in NED.

Magnitudes were adopted from NED for two spiral galaxies (ESO 274-01 and NGC 247, see Table 2) which were extending beyond the ACS field of view as well as for NGC 4605 which was off-center and for KKH 77 which was contaminated by a very bright (and saturated) foreground star. These magnitudes from NED are (deprojected) total magnitudes corrected for internal reddening assuming $E_{B-V} = 0.05$ mag. For IKN and VKN, two extremely low surface brightness dwarfs ($M_V \approx -11.5$ and -10.5 mag, respectively), we could not reliably determine their magnitudes due to an extremely bright foreground star in the former and the very low surface brightness of the latter (close to the level of background fluctuations and measurement errors). Their $V-$band magnitudes were derived from their $B-$band magnitudes assuming an average $B - V = 0.45$ mag estimated from the rest of the dwarfs. Due to the fact that UGCA 86 was centered in the middle of ACS chip 2, its Holmberg radius extended beyond the ACS field by $\sim 1'$ and, therefore, we had to extrapolate its magnitude with the gradient of the last 3 magnitude bins of its curve of growth.

Finally, the derived magnitudes were compared with the published ones for six dwarfs in our sample (DDO 52, ESO 269-58, IC 4662, NGC 5237, 4068, 4163) and found consistent within the measurement errors. The magnitudes of all galaxies are listed in Table 2.

3.2 Color Distributions

In Figure 4 we show the color-magnitude diagrams for GCs in dIrr, dE/dSph, and Sm galaxies, and the composite sample, combining the results from this work with our identically analyzed sample from Georgiev et al. (2008). The color and luminosity distributions are illustrated as histograms in the top and right sub-panels, where the curves indicate non-parametric Epanechnikov kernel probability density estimates. We subdivide the samples in color into blue GCs (bGCs) with $V-I \leqslant 1.0$ mag and red GCs (rGCs) with $V-I > 1.0$ mag, which include the sub-sample of extremely red objects with colors $V-I > 1.4$ mag[8]. This division is motivated by the average location of the gap between the blue and red color peaks of rich GCSs in massive early-type galaxies (e.g. Gebhardt & Kissler-Patig 1999).

An intriguing feature of Figure 4 is the lack of faint ($M_V \gtrsim -6$) blue GCs in our sample dIrr galaxies. Our artificial cluster tests show that this is not a completeness effect as our 90% completeness limit is at $M_V = -4.5$ mag (see Sect. 2.5). Finding one or more GCs in these faint dwarfs would increase their already high specific frequencies even more (the specific frequencies will be discussed in a subsequent paper of this series). On the other hand, we do observe few clusters at $M_V \simeq -5.5$ to -6.5 mag and $(V-I) < 1.0$ mag in galaxies with dE/dSph and Sm morphology[9].

One plausible explanation for the apparent lack of faint blue clusters is that the metal-poor ($V - I < 1.0$ mag) and low-mass GCs ($M_V > -6.5$ mag) are actually younger (age < 4 Gyr) than our selection criteria. If this is spectroscopically confirmed would imply that GCs in dIrrs formed a bit later than GCs in more massive early-type galaxies. To explore this effect we investigate stellar evolution fading according to the SSP model of Bruzual & Charlot (2003). Passive aging of a simple stellar population from 3 to 14 Gyr red-

---

[7] http://heasarc.nasa.gov/W3Browse/all/hubbleudf.html

[8] The faintest clusters with $M_V \leqslant -6$ and $(V-I)_0 > 1.0$ mag are likely background contaminants which passed our selection criteria. Their nature will be confirmed by follow-up spectroscopy.

[9] We note that all absolute magnitudes were calculated using the newly determined distance moduli by Tully et al. (2006) and Karachentsev et al. (2006, 2007) which are fainter by ~ 0.5 mag on average from the values listed in Karachentsev et al. (2004), hence, the GCs have brighter absolute magnitudes.

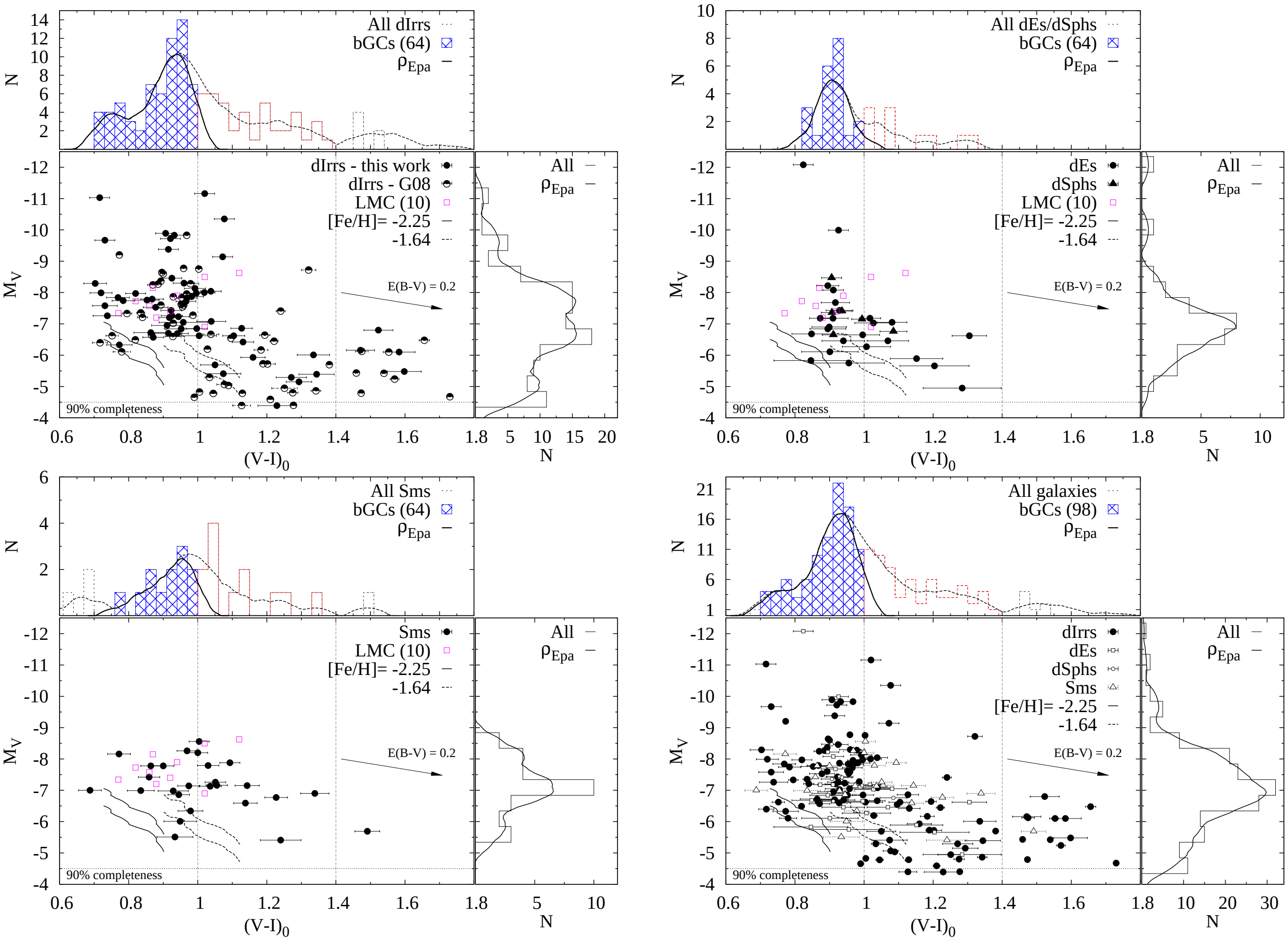

Figure 4. Combined color-magnitude diagrams for GC candidates in our sample galaxies split by the morphological type of the host. GCs in dIrr galaxies are shown in the upper left panel; the other panels show the corresponding distributions for dEs/dSphs, Sm, and of the combined sample. Filled and semi-filled circles in the dIrr-panel indicate GC candidates from the current and Georgiev et al. (2008) study. Open squares are old LMC GCs (data from McLaughlin & van der Marel 2005). The vertical dotted lines mark the color separating blue and red GC candidates at $V-I=1.0$ mag. Thick solid and dashed curves show Bruzual & Charlot (2003) SSP evolutionary tracks for two clusters masses $M_{\rm cl}=3\cdot10^4$ and $5\cdot10^4\,M_\odot$ from 3 to 14 Gyr (left to right) and metallicities [Fe/H] $=-2.25$ and -1.64 dex, respectively. Histograms illustrate the GC candidate color and luminosity distributions. A reddening vector shows the effect of $E_{B-V}=0.2$ of internal extinction.

dens its $(V-I)_0$ color by ~0.15 mag and fades its $V-$band luminosity by ~1.5 mag. This is illustrated in Figure 4 with evolutionary tracks for two metallicities ([Fe/H] $=-2.25$ and -1.64 dex) and two cluster masses ($M_{\rm cl}=3\cdot10^4$ and $5\cdot10^4\,M_\odot$) If some of the bluest GCs in our sample are indeed younger clusters (with $t\lesssim4$ Gyr) they will end up on the faint-end of the luminosity function at an age of 14 Gyr. However, those clusters would have to have unusually low metallicities ([Fe/H] $\leqslant-2.0$), an interesting result that calls for spectroscopic confirmation. Previous spectroscopic analyses of GCs in other dwarf galaxies show that their blue colors are in general consistent with old ages and low metallicities. However, some of these clusters show spectroscopic intermediate ages (~4 Gyr), in particular in dIrrs (Puzia & Sharina 2008). An alternative (though perhaps less likely) explanation for the lack of old, metal-poor, low-mass clusters in dIrr galaxies may be selective reddening of such objects. The reddening vector in the CMDs of Figure 4 shows that a reddening of $E_{B-V}=0.2$ mag is enough to dislocate intrinsically blue GCs to the red GC sub-sample. The age and reddening effects should be tested with spectroscopic observations.

The probability density estimates, as shown in Figure 4, for all galaxy subsamples give the highest probability values in the range $(V-I)_{0,\rho}\approx0.9-1.0$ mag and $M_{V,\rho}\approx-7.5$ to -6.5 mag. Gaussian fits to the smoothed bGC luminosity function give peak values in the range $M_{V,{\rm TO}}=-7.6$ to -7.0 mag with $\sigma_{\rm GCLF}=1.2-1.5$ mag (see Sect. 3.3). The color distributions of GCs in our sample galaxies peak at values typically found in other low-mass dwarfs (Seth et al. 2004; Sharina et al. 2005; Georgiev et al. 2006, 2008), and are very similar to the canonical blue peak color of rich GCSs in massive early-type galaxies (e.g. Peng et al. 2008). For comparison we also show ten of the brightest old LMC GCs (McLaughlin & van der Marel 2005). There are three

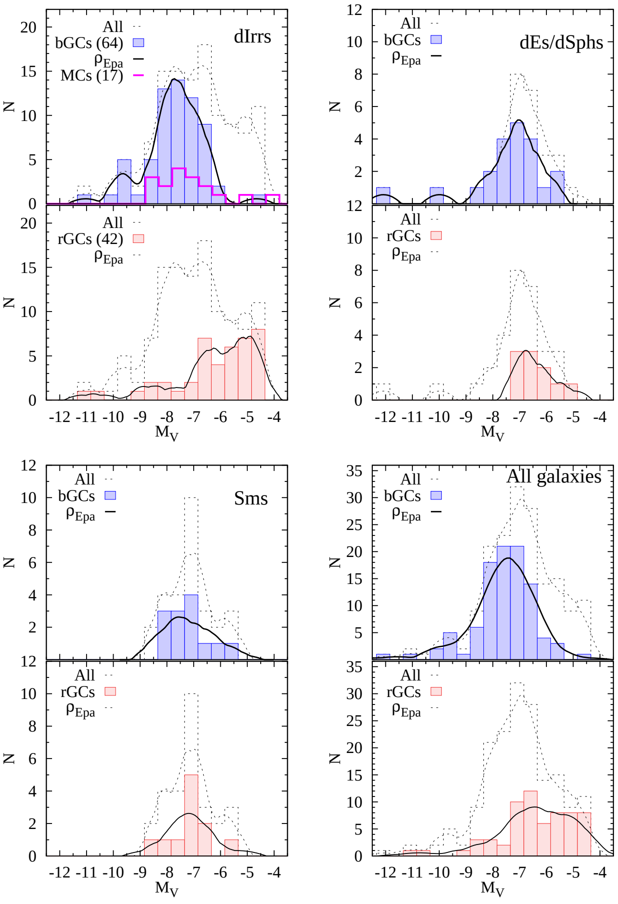

Figure 5. Luminosity distributions of selected blue and red GCs in the top and bottom panels, respectively. Each sub-sample was split at $V-I=1.0$ mag in bGCs and rGCs. Shaded histograms show the corresponding GC candidates luminosity distribution, while open histograms are the total samples for a given host morphology. In all panels, thick and dotted curves are non-parametric Epanechnikov-kernel probability density estimates. The solid line open histogram shows in the upper left panel the luminosity distribution of old LMC GCs for comparison (data from McLaughlin & van der Marel 2005).

more LMC clusters that are fainter than $M_V=-6.5$ mag, however, without available $V-I$ colors.

3.3 Luminosity Functions

Figure 5 shows the luminosity functions of the blue and red GCs in the top and bottom sub-panels, respectively, which were split at $V-I=1.0$ mag. Thick curves are Epanechnikov kernel probability density estimates. We find that the rGCs are biased toward fainter luminosities compared to the bGC sub-sample. This indicates that these objects are either strongly affected by background contamination or intrinsically fainter than their bGC counterparts. Gaussian fits to the smoothed histogram distributions return $M_{V,\rm TO}=-7.56\pm0.02$ mag and $\sigma_{\rm GCLF}=1.23\pm0.03$ for dIrr, $M_{V,\rm TO}=-7.04\pm0.02$ mag and $\sigma_{\rm GCLF}=1.15\pm0.02$ for dE/dSph, and $M_{V,\rm TO}=-7.30\pm0.01$ mag and $\sigma_{\rm GCLF}=1.46\pm0.02$ for Sm galaxies (note the different sample sizes when comparing sub-populations in Fig. 5). Assuming a typical $M/L_V=1.8$ obtained for old metal-poor Magellanic GCs (McLaughlin & van der Marel 2005) the turnover magnitude translates to a turnover mass $m_{\rm TO}\simeq1.6\times10^5\,{\rm M}_\odot$, in excellent agreement with the results of Jordán et al. (2007).

The GC luminosity function turn over magnitude for dIrrs is slightly brighter than those for dE/dSph and Sm galaxies, and it shows significantly broader luminosity function peaks extending to fainter magnitudes. This may be due to the interplay of different formation mechanisms and ages/metallicities or perhaps due to contamination by background galaxies. In general, all $M_{V,\rm TO}$ values are consistent with the luminosity function turn-over magnitude for metal-poor Galactic GCs (Di Criscienzo et al. 2006), as well as for GCs in early-type dwarfs (Sharina et al. 2005; Jordán et al. 2007; Miller & Lotz 2007), and virtually identical to the turn-over magnitude of old LMC GCs at $M_V=-7.50\pm0.16$ mag (data from McLaughlin & van der Marel 2005).

3.4 Nucleated Dwarf Irregular Galaxies

Another interesting feature in the CMDs of Figure 4 is the presence of a few relatively bright GCs in dIrr and dE/dSph galaxies, which are similar in color and magnitude to ω Cen and M 54. Those clusters are located in the nuclear regions of their host galaxies. Such bright objects do not appear in the Sm sub-sample. A dedicated study of the properties of these bright GCs will be presented in a forthcoming paper of this series.

3.5 Structural Parameters

Since the clusters' half-light radii, $r_{\rm h}$, and ellipticities, ϵ, are stable over many relaxation times (e.g. Spitzer & Thuan 1972) and, thus, contain information about the initial conditions and the dynamical evolution of clusters over a Hubble time. In particular, the cluster half-light radius is stable during >10 relaxation times (i.e., ~10 Gyr) (e.g. Aarseth & Heggie 1998), while the ellipticity decreases by a factor of two within five relaxation times and reaches asymptotic values around 0.1 (Fall & Frenk 1985; Han & Ryden 1994; Meylan & Heggie 1997).

3.5.1 Half-Light Radii

In Figure 6 we present the measurements of $r_{\rm h}$ for GCs in our sample galaxies. The majority of GCs lies below the empirically established relation $\log r_{\rm h}=0.25\times M_V+2.95$ (Mackey & van den Bergh 2005), which forms the upper envelope of Galactic GCs in the M_V vs. $r_{\rm h}$ plane (see lower left sub panels in Fig. 6). Some of these brightest GCs, that reside in the nuclear regions of their hosts, tend to lie on or above that envelope (towards larger r_h at a given M_V), which seems typical for nuclear star clusters (e.g. Böker et al. 2004; Haşegan et al. 2005). This region is also occupied by the peculiar Galactic GCs ω Cen, NGC 2419, NGC 2808, NGC 6441 and M 54, the nucleus of the Sagittarius dSph galaxy. For an object with high S/N (>50) and good knowledge of the PSF, the theoretical spatial resolution limit can be as good as 10% of the PSF (~0.2 pix for ACS/PSF) (Larsen 1999). Thus, at the median distance of the entire galaxy sample of ~5 Mpc and taking into account the $r_{\rm h}$ measurement error, the spatial resolution can be as

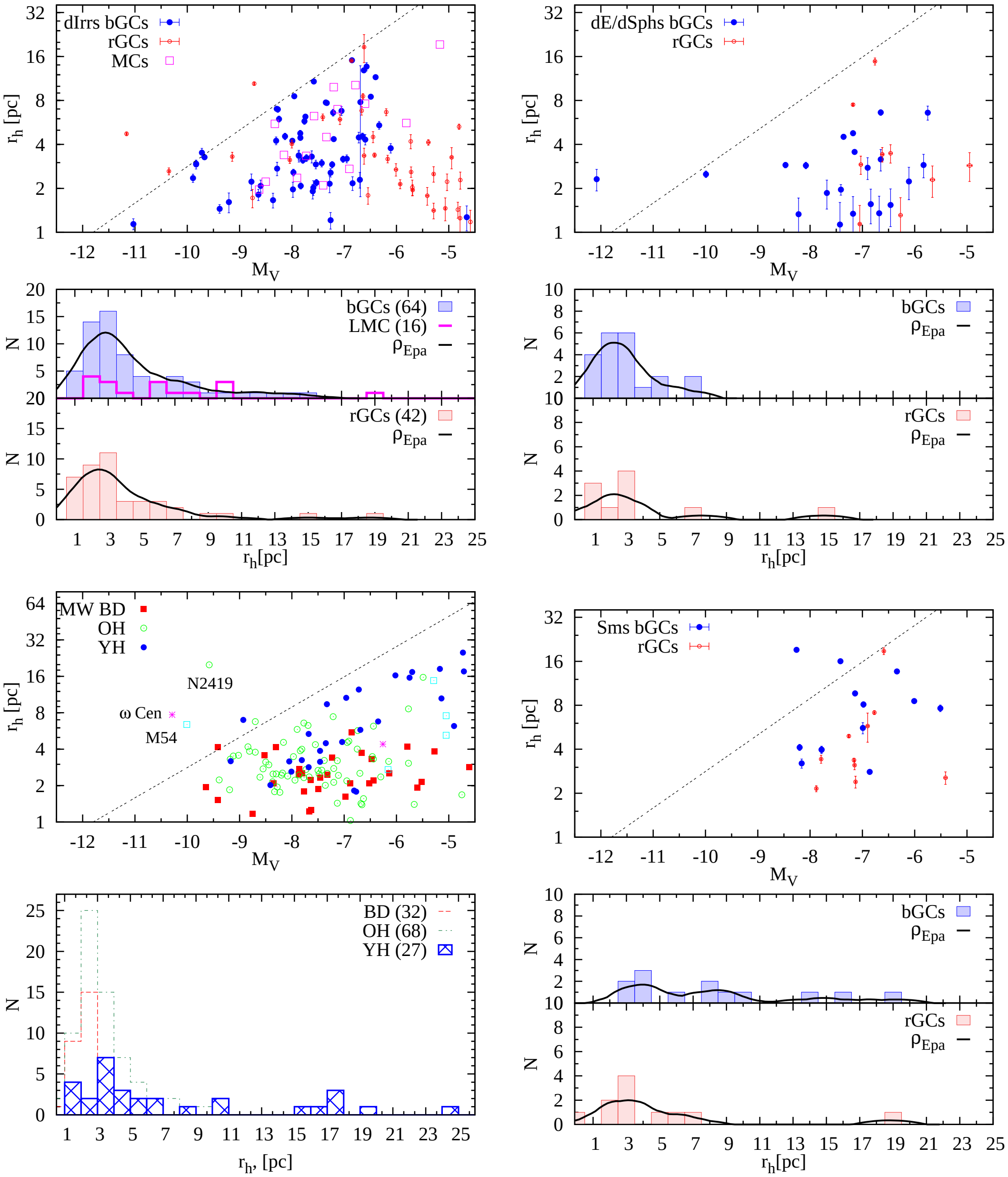

Figure 6. Luminosity M_V versus half-light radius $r_{\rm h}$ for GCs in dIrrs *upper left panel*, dE/dSph *upper right panel*, and Sm galaxies *lower right panel*. Each sub-sample was split at $V-I=1.0$ mag in bGCs and rGCs. In the upper left panel we show old GCs in the Magellanic Clouds (McLaughlin & van der Marel 2005). The dashed line indicates the upper envelope for the distribution of Galactic GCs (Mackey & van den Bergh 2005). The lower sub-panels show the corresponding $r_{\rm h}$ distributions for the blue and red GC candidates. The thick curves are Epanechnikov-kernel probability density estimates. Note that in all our sub-samples the $r_{\rm h}$ distributions of blue GCs appears more extended than that of the red GCs.

good as ~ 0.9 pc (~ 0.8 pix). Therefore, the majority of the clusters with high S/N are well resolved, even for the distant most galaxy in our sample at ~ 12 Mpc.

The half-light radius distribution of the bGCs and rGCs is shown in the bottom sub-panels of Figure 6. On average, bGCs appear more extended than rGCs in all sub-samples, by about 9%, however with low statistical significance. On average, the most compact bGC population is found in dE/dSph host galaxies ($r_{\rm h,med} = 2.5$ pc), followed by bGCs in dIrrs ($r_{\rm h,med} = 3.3$ pc) and Sm galaxies ($r_{\rm h,med} = 7.6$ pc), whose GC population is more incomplete due to the restricted spatial coverage (cf. Sect. 3.1). We find the highest value of the probability density estimate of the entire sample at $r_{\rm h} \approx 2.9$ pc and a median $r_{\rm h,med} = 3.2 \pm 0.5$ pc. These values are typical for Galactic GCs (Harris 2001). The median value of the old LMC GCs is $r_{\rm h,med} = 5$ pc (based on measurements from McLaughlin & van der Marel 2005).

A comparison between the $r_{\rm h}$ distribution of the total bGC sample with the sizes of different metal-poor, Galactic GC sub-populations shows that the old halo (OH) GCs have

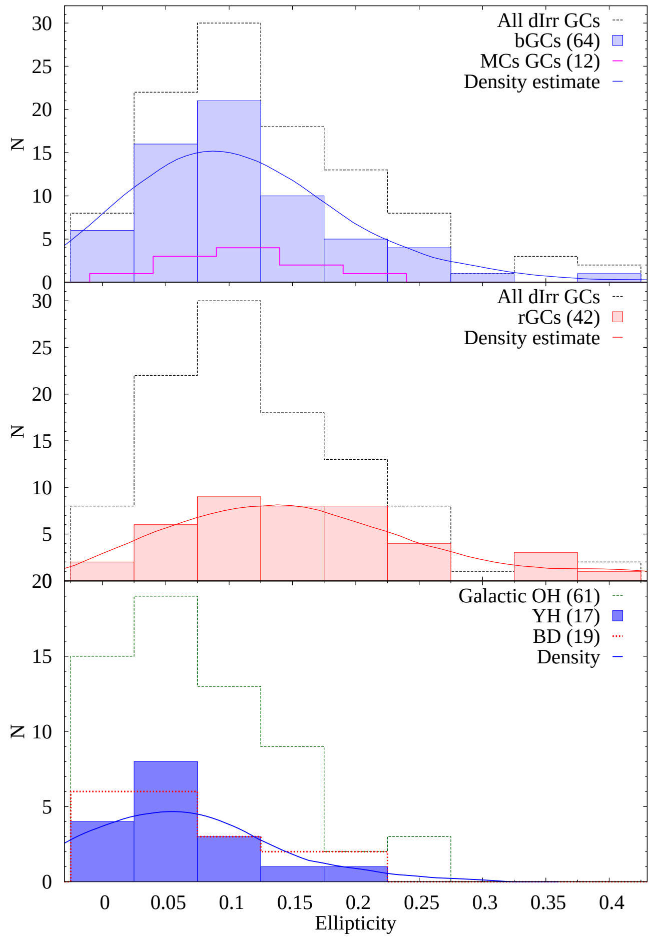

Figure 7. Ellipticity ($\epsilon = 1 - b/a$) distributions of GCs in dwarf irregular galaxies. The top panel shows that bGCs in our sample dIrrs and in LMC are similarly flattened. The even broader ϵ distribution for the rGCs shows that the majority are likely background contaminants. The bottom panel shows the ϵ distribution for the Galactic GC subpopulations: OH = Old Halo; YH = Young Halo; BD = Bulge/Disk.

comparable ($r_{\mathrm{h,med}} = 3\,\mathrm{pc}$) and the young halo (YH) GCs have larger median sizes ($r_{\mathrm{h,med}} = 5.4\,\mathrm{pc}$) than blue GCs in our sample dwarf galaxies. We note, however, that if all Galactic GCs are considered, there is practically no difference in the mean r_{h} . In the light of the accretion origin of the YH-GCs, their r_{h} might have been influenced by the change of the host potential, which leads to an increase of the cluster r_{t} at large Galactocentric distances, and disk/bulge shocking causing mass loss, thus toward lower masses and larger r_{h} (cf Fig. 8, Sect. 3.6). This is supported by the high orbital energy ($\mathrm{E}_{\mathrm{tot}}$, $\mathrm{Z}_{\mathrm{max}}$, eccentricity, velocity, angular momentum) found for YH-GCs (Lee et al. 2007) which also supports an accretion origin of those.

3.5.2 Ellipticities

A difference between bGCs in dIrrs and those of the various Galactic GC sub-populations is also found when clusters ellipticities are compared. In Figure 7 we show the ellipticity distribution of GCs in our sample dIrrs and in the Magellanic Clouds for which we used data from Frenk & Fall (1982) and Kontizas et al. (1989, 1990). The non-parametric kernel density estimate identifies peaked distributions with values $\epsilon \simeq 0.1$ for both samples. This is a markedly different ellipticity distributon than that of Galactic GCs which is biased towards lower ellipticity values.

Fall & Frenk (1985) showed for self-gravitating clusters that during a period $\sim 5t_{\mathrm{rh}}$ the ellipticity, ϵ, decreases by a factor of two and reaches an asymptotic value of $\epsilon \simeq 0.1$, corresponding to the observed mean ellipticity of our bGCs in dIrr galaxies. Under the assumption that the ages of the (bulk of the) GCs in our dIrr galaxies are similar to those of Galactic GCs, this implies that our sample bGCs as well as the MC old GCs evolved dynamically in isolation (i.e. mainly affected by internal processes rather than external cluster dissolution processes).

The broad ellipticity distribution of the rGCs, which extends toward large values, indicates that many or most of them are likely background contaminants.

3.6 Dynamical State of Star Clusters in Dwarf Galaxies

The r_{h} versus cluster mass plane (Fig. 8) is often used to illustrate cluster "survivability" that depends on the interplay between various external and internal dissolution mechanisms (e.g. Fall & Rees 1977; Gnedin & Ostriker 1997; Fall & Zhang 2001; McLaughlin & Fall 2008). In Figure 8 we show the distribution of all sample GCs in this plane together with GCs in the Galaxy and the Magellanic Clouds (MCs). To convert from luminosities to masses we adopt a mean $M/L_V = 1.8$ derived for the old MC clusters (McLaughlin & van der Marel 2005). The half-light radius estimates and cluster masses for MC and Galactic clusters were taken from McLaughlin & van der Marel (2005), where available, and from Harris (1996) for the remainder. It should be noted, however, that if the GCs in our sample are on average younger, their M/L−ratios would be smaller.

In the following we discuss the influence of the various dynamical effects on the evolution of our sample GCs. Dash-dotted lines show the cluster evaporation limit due to two-body relaxation (Fall & Rees 1977; Spitzer 1987; Gnedin & Ostriker 1997)

$$r_{\mathrm{h}} = \left(\frac{12\,000[\mathrm{Myr}]}{20}\right)^{2/3}\left(\frac{0.138}{\sqrt{G}m_\star \ln\left(\gamma\frac{M}{m_\star}\right)}\right)^{-2/3} M^{-1/3} \quad (1)$$

for clusters that survived 12 Gyr after 20 initial relaxation times; $m_\star = 0.35 M_\odot$ is the average stellar mass in a GC after 12 Gyr of evolution and $\gamma = 0.02$ is a correction constant taken from models which simulate clusters with a specific mass spectrum (Giersz & Heggie 1996). GCs with r_{h} values lower values than this "survival" limit will have dissolved after a Hubble time of dynamical evolution (e.g. Fall & Zhang 2001).

The evolution of a star cluster in the Galactic tidal field was investigated by Baumgardt & Makino (2003). We have used their equation 7 to calculate the minimum mass of a cluster which can survive for 12 Gyr within a mean projected distance of $d_{\mathrm{proj}} \approx 0.8\,\mathrm{kpc}$ from the galaxy center, matching the average d_{proj} of GCs in our sample. The result is shown as the left vertical dashed line in Figure 8 and corresponds to

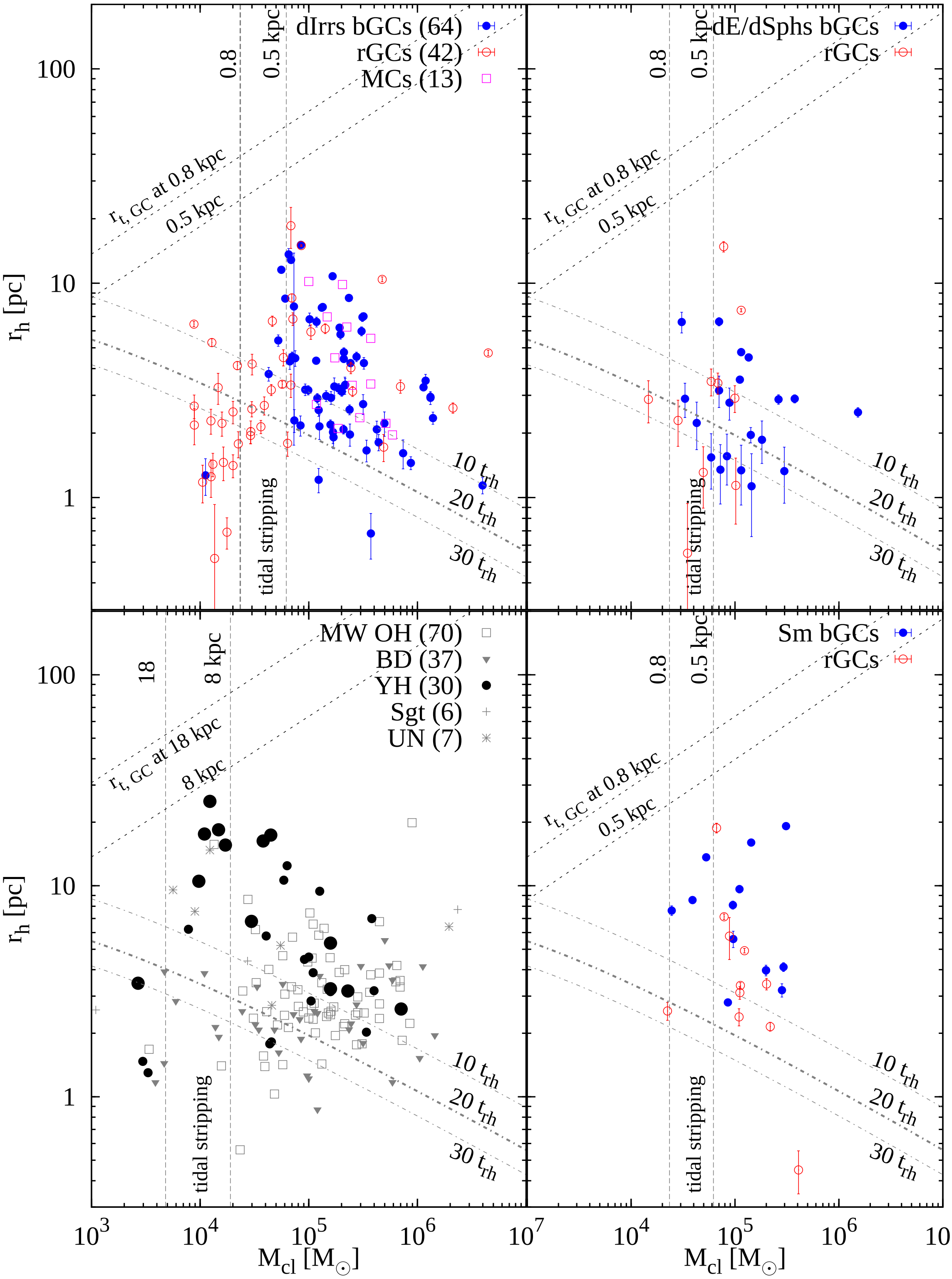

Figure 8. Half-light radius versus custer mass for GCs in low-mass galaxies. The panels show from the top left panel clockwise: bGCs and rGCs (filled and open circles) in dIrr galaxies (split at $V-I = 1.0$ mag) and old Magellanic Clouds GCs (open squares); GCs in dE/dSph galaxies, GCs in Sm galaxies; the lower left panel shows the Galactic YH-GCs, which were split according to their galactocentric distance being larger or smaller than 18 kpc (large or small filled circles, respectively), and OH and BD GCs (open squares and filled triangles), Sagittarius dwarf GCs (plus signs), and clusters with unknown classification (asterisk). Lines indicate theoretical predictions for cluster dissolution over a Hubble time due to tidal field effects for clusters at 0.8 and 0.5 kpc from the center of the host (left and right vertical lines, respectively), two-body relaxation processes as well as cluster re-expansion after (dash-dotted lines), (for details see Sect. 3.6). With dotted lines are also shown the cluster tidal radius ($r_{t,GC}$) at two assumed galactocentric distances (0.5 and 0.8 kpc). Note that the larger error bars in the dE/dSph panel are GCs in one of the most distant galaxies in our sample - the dE UGC 7369 at 11.6 Mpc.

a minimum mass of $\sim 2.3 \times 10^4 M_\odot$ ($M_V = -5.5$ mag). Clusters below this mass limit would have dissolved in the tidal field of the dwarf galaxy after a Hubble time of evolution. The right vertical line indicates the minimum cluster mass for $d_{\rm proj} = 0.5$ kpc. It should be mentioned, however, that effects due to a variable tidal field and dynamical friction were not taken into account. Vesperini (2000) showed that low-mass galaxies efficiently disrupt the majority ($\sim$ 90%) of their initial star-cluster population due to dynamical friction.

An interesting aspect of cluster evolution is the re-expansion of star clusters that can occur after the process of core collapse. The time evolution of cluster mass and half-light radius is

$$M(t) = M_0 \left(\frac{t}{t_0}\right)^{-\nu} \quad \text{and} \quad r_{\rm h}(t) = r_{\rm h_0} \left(\frac{t}{t_0}\right)^{\frac{2+\nu}{3}} \qquad (2)$$

and was first obtained by Hénon (1965), where $M = M_{cl}/m_\star$ and M_0 and $r_{\rm h_0}$ are the cluster mass and half-light radius at the time of core collapse t_0 and $\nu = 0.01 - 0.1$ (Baumgardt et al. 2002) is the dynamical mass-loss factor. Combining both equations one obtains

$$r_{\rm h} = r_{\rm h0} \left(\frac{M}{M_0}\right)^{-\frac{2+\nu}{3\nu}} \qquad (3)$$

Since core collapse occurs within several initial cluster relaxation times $t_0 = n_{\rm rh} t_{\rm rh,i}$ (see Gieles & Baumgardt 2008) we can combine Equations 1 and 3 and obtain

$$r_{\rm h} = (t_0)^{2/3} \left(\frac{0.138}{\sqrt{G} m_\star \ln\left(\gamma \frac{M_0}{m_\star}\right)}\right)^{-2/3} M_0^{-1/3} \left(\frac{M}{M_0}\right)^{-\frac{2+\nu}{3\nu}} \qquad (4)$$

Consequently, if $M_0 = M$ (i.e. no dynamical mass-loss after core collapse) at $t_0 = t = 12$ Gyr ($\sim$Hubble time), and $n_{\rm rh} = 20$ the equation yields the limit labeled "$20 t_{\rm rh}$" in Figure 8. A cluster that starts its evolution below this relation will be prone to expansion with a likely depletion of cluster stars prior to 20 relaxation times. In summary, the distribution of GCs in all studied dwarfs shows that their dynamical evolution was governed by internal processes (two-body relaxation, stellar evolution). The absence of GCs at masses lower than the lower mass limit due to disruption by the galactic tidal field within the mean projected radius of the GCs in the sample galaxies ($\sim 3\times 10^4 M_\odot$, see Fig. 8) suggests that tidal disruption was important as well. With dotted lines are in Figure 8 are shown the cluster tidal radius at two galactocentric distances, 0.5 and 0.8 kpc for the dwarfs in our sample and at 8 and 18 kpc for Galactic clusters. This sets up an upper limit to the cluster size. The different distribution of rGCs with respect to that of bGCs in Fig. 8 indicates that most rGCs are background contaminants.

The comparison between our GC sample and Galactic GCs (bottom left panel in Fig. 8) shows that bGCs, MC GCs, and Galactic YH GCs share very similar distributions, which suggests that those objects have experienced similar formation and/or dynamical evolution in the weak tidal fields of the dwarf and the Milky Way halo regions. In contrast, the Galactic OH and BD clusters show distributions that are significantly different from those of dwarf galaxy bGCs and Galactic YH GCs. This may indicate that their dynamical evolution was affected by the stronger inner Galactic tidal field and disk/bulge shocking.

4 CONCLUSIONS

We present the analysis of archival F606W and F814W HST/ACS data for 68 low-mass faint ($M_V > -16$ mag) dwarf galaxies located in the halo regions of nearby ($\lesssim$ 12 Mpc), loose galaxy groups. Most of the dwarf galaxies in our sample are more than 2 mag fainter than the LMC ($M_V = -18.36$ mag) and just as bright as the SMC ($M_V = -16.82$ mag). The morphological makeup of our sample, summarized in Table 1, comprises 55 dIrrs, 3 dEs, 5 dSphs and 5 low-mass late-type dwarf spirals. Old GC candidates were found in 30 dIrrs, 2 dEs, 2 dSphs and in 4 Sms. In total we found 175 GC candidates and measure their colors and magnitudes which are consistent with old and metal-poor stellar populations. The total sample contains 97 blue GCs ($0.7 < (V-I)_0 < 1.0$ mag) GCs, 63 red GCs ($1.0 < (V-I)_0 < 1.0$ mag) with the rest being very red ($(V-I)_0 > 1.0$ mag) likely background contaminants.

The combined color distribution of GCs in dIrrs peaks at $(V-I) = 0.96 \pm 0.07$ mag and the GC luminosity function turnover is at $M_{V,TO} = -7.6$ mag, similar to the old LMC GCs. Gaussian fits to the smoothed histogram distributions return $M_{V,\rm TO} = -7.56 \pm 0.02$ mag and $\sigma = 1.23 \pm 0.03$ for dIrrs, $M_{V,\rm TO} = -7.04 \pm 0.02$ mag and $\sigma = 1.15 \pm 0.03$ for dE/dSph, and $M_{V,\rm TO} = -7.30 \pm 0.01$ mag and $\sigma = 1.46 \pm 0.02$ for Sm galaxies. We thus find a tentative trend of $M_{V,\rm TO}$ becoming fainter from late-type to early-type dwarf galaxies. Our artificial cluster tests show that this trend is not due to incompleteness and may reflect relatively younger GC systems in dIrrs by $\sim 2-5$ Gyr depending on the metallicity. If confirmed, this would imply that GCs in dIrrs formed later than blue GCs in massive galaxies. Thus we suggest that this result be followed-up with spectroscopic observations.

The comparison of GC structural parameters with theoretical cluster disruption models (including dynamical processes, such as stellar mass loss, relaxation, tidal shocking indicates that the dynamical evolution of blue GCs in our sample is consistent with the evolution of self-gravitating systems in a weak tidal field. Their half-light radii and cluster masses evolve primarily due to two-body relaxation. The $r_{\rm h}$ vs. cluster mass plane shows a similar distribution between bGCs in our sample and Galactic Young Halo (YH) clusters, which is indicative of a similar formation and dynamical evolution history. Dynamical models of star clusters evolving in isolation show that they reach an asymptotic ellipticity $\epsilon \approx 0.1$ after few cluster relaxation times ($> 5 t_{\rm rh}$). Our analysis reveals that bGCs in our sample galaxies on average more flattened ($\bar{\epsilon} = 0.1$) than Galactic GCs, but have a similar ellipticity distribution as GCs in the LMC. This suggests that old GCs in low-mass galaxies are dynamically evolved stellar systems that spent most of their evolution in benign tidal environment.

We briefly report on the discovery of several bright (massive and/or young) GCs in the nuclear regions of some dIrr and dSph galaxies. These massive nuclear clusters show similar structural parameters as the peculiar Galactic clusters suspected of being the remnant nuclei of accreted dwarf galaxies, such as M 54 and ωCen. If such accretion events happened early in the assembly history of the Galaxy, any tidal streams from the host low-surface brightness dIrr galaxies would likely have largely dissolved by now and thus escape detection. We will present a more detailed analysis of the properties of the nuclear clusters in a forthcoming paper in this series.

ACKNOWLEDGMENTS

IYG is grateful for the award of a STScI Graduate Research Fellowship, and acknowledges support from the German Science Foundation through the grant DFG-Projekt BO-779/32-1. THP acknowledges financial support from the National Research Council of Canada in form of the Plaskett Research Fellowship. Based on observations made with the NASA/ESA Hubble Space Telescope, and obtained from the Hubble Multimission Archive, which is a collaboration between the Space Telescope Science Institute (STScI/NASA), the Space Telescope European Coordinating Facility (ST-ECF/ESA) and the Canadian Astronomy Data Centre (CADC/NRC/CSA).

The authors are very thankful to the referee for the careful and thorough reading whose suggestions improved the paper. We would also like to thank Holger Baumgardt for the valuable discussions.

REFERENCES

Aarseth S. J., Heggie D. C., 1998, MNRAS, 297, 794
Anders P., Fritze-v. Alvensleben U., 2003, A&A, 401, 1063
Ashman K. M., Zepf S. E., 1992, ApJ, 384, 50
Baumgardt H., Hut P., Heggie D. C., 2002, MNRAS, 336, 1069
Baumgardt H., Makino J., 2003, MNRAS, 340, 227
Beasley M. A., Baugh C. M., Forbes D. A., Sharples R. M., Frenk C. S., 2002, MNRAS, 333, 383
Bekki K., Forbes D. A., Beasley M. A., Couch W. J., 2002, MNRAS, 335, 1176
Böker T., Sarzi M., McLaughlin D. E., van der Marel R. P., Rix H.-W., Ho L. C., Shields J. C., 2004, AJ, 127, 105
Brodie J. P., Strader J., 2006, ARA&A, 44, 193
Bruzual G., Charlot S., 2003, MNRAS, 344, 1000
Conselice C. J., Rajgor S., Myers R., 2008, MNRAS, pp 446–+
Côté P., Marzke R. O., West M. J., 1998, ApJ, 501, 554
Côté P., West M. J., Marzke R. O., 2002, ApJ, 567, 853
Da Costa G. S., Armandroff T. E., 1990, AJ, 100, 162
Di Criscienzo M., Caputo F., Marconi M., Musella I., 2006, MNRAS, 365, 1357
Durrell P. R., Harris W. E., Geisler D., Pudritz R. E., 1996, AJ, 112, 972
Fall S. M., Frenk C. S., 1985, in Goodman J., Hut P., eds, Dynamics of Star Clusters Vol. 113 of IAU Symposium, Rotation and flattening of globular clusters. pp 285–296
Fall S. M., Rees M. J., 1977, MNRAS, 181, 37P
Fall S. M., Zhang Q., 2001, ApJ, 561, 751
Forbes D. A., Brodie J. P., Grillmair C. J., 1997, AJ, 113, 1652
Frenk C. S., Fall S. M., 1982, MNRAS, 199, 565
Gebhardt K., Kissler-Patig M., 1999, AJ, 118, 1526
Georgiev I. Y., Goudfrooij P., Puzia T. H., Hilker M., 2008, AJ, 135, 1858
Georgiev I. Y., Hilker M., Puzia T. H., Chanamé J., Mieske S., Goudfrooij P., Reisenegger A., Infante L., 2006, A&A, 452, 141
Gieles M., Baumgardt H., 2008, astro-ph/0806.2327, 806
Giersz M., Heggie D. C., 1996, MNRAS, 279, 1037
Gnedin O. Y., Ostriker J. P., 1997, ApJ, 474, 223
Goudfrooij P., Mack J., Kissler-Patig M., Meylan G., Minniti D., 2001, MNRAS, 322, 643
Goudfrooij P., Schweizer F., Gilmore D., Whitmore B. C., 2007, AJ, 133, 2737
Goudfrooij P., Strader J., Brenneman L., Kissler-Patig M., Minniti D., Edwin Huizinga J., 2003, MNRAS, 343, 665
Grillmair C. J., 2006, ApJL, 651, L29
Haşegan M., Jordán A., Côté P., Djorgovski S. G., McLaughlin D. E., Blakeslee J. P., Mei S., West M. J., Peng E. W., Ferrarese L., Milosavljević M., Tonry J. L., Merritt D., 2005, ApJ, 627, 203
Han C., Ryden B. S., 1994, ApJ, 433, 80
Harris W. E., 1996, AJ, 112, 1487
Harris W. E., 2001, in Labhardt L., Binggeli B., eds, Saas-Fee Advanced Course 28: Star Clusters Globular cluster systems. pp 223–+
Harris W. E., 2003, in Kissler-Patig M., ed., Extragalactic Globular Cluster Systems Issues in E Galaxy Formation: Many Problems, Few Solutions. pp 317–+
Harris W. E., Harris G. L. H., 2002, AJ, 123, 3108
Harris W. E., Harris G. L. H., Barmby P., McLaughlin D. E., Forbes D. A., 2006, AJ, 132, 2187
Harris W. E., van den Bergh S., 1981, AJ, 86, 1627
Harris W. E., Whitmore B. C., Karakla D., Okoń W., Baum W. A., Hanes D. A., Kavelaars J. J., 2006, ApJ, 636, 90
Hénon M., 1965, Annales d'Astrophysique, 28, 62
Hilker M., Infante L., Richtler T., 1999, A&AS, 138, 55
Ibata R., Irwin M., Lewis G., Ferguson A. M. N., Tanvir N., 2001, Nature, 412, 49
Ibata R. A., Gilmore G., Irwin M. J., 1994, Nature, 370, 194
Jordán A., Côté P., Blakeslee J. P., Ferrarese L., McLaughlin D. E., Mei S., Peng E. W., Tonry J. L., Merritt D., Milosavljević M., Sarazin C. L., Sivakoff G. R., West M. J., 2005, ApJ, 634, 1002
Jordán A., McLaughlin D. E., Côté P., Ferrarese L., Peng E. W., Mei S., Villegas D., Merritt D., Tonry J. L., West M. J., 2007, ApJS, 171, 101
Karachentsev I. D., Dolphin A., Tully R. B., Sharina M., Makarova L., Makarov D., Karachentseva V., Sakai S., Shaya E. J., 2006, AJ, 131, 1361
Karachentsev I. D., Karachentseva V. E., Huchtmeier W. K., Makarov D. I., 2004, AJ, 127, 2031
Karachentsev I. D., Tully R. B., Dolphin A., Sharina M., Makarova L., Makarov D., Sakai S., Shaya E. J., Kashibadze O. G., Karachentseva V., Rizzi L., 2007, AJ, 133, 504
Khochfar S., Silk J., Windhorst R. A., Ryan Jr. R. E., 2007, ApJL, 668, L115
Kissler-Patig M., 2000, in Schielicke R. E., ed., Reviews in Modern Astronomy Extragalactic Globular Cluster Systems: A new Perspective on Galaxy Formation and Evolution. pp 13–+
Kissler-Patig M., Kohle S., Hilker M., Richtler T., Infante L., Quintana H., 1997, A&A, 319, 470

Koekemoer A. M., Fruchter A. S., Hook R. N., Hack W., 2002, in Arribas S., Koekemoer A., Whitmore B., eds, The 2002 HST Calibration Workshop MultiDrizzle: An Integrated Pyraf Script for Registering, Cleaning and Combining Images. pp 337–+

Kontizas E., Kontizas M., Sedmak G., Smareglia R., 1989, AJ, 98, 590

Kontizas E., Kontizas M., Sedmak G., Smareglia R., Dapergolas A., 1990, AJ, 100, 425

Krist J., Hook R., 2004, "The TinyTim Manual": . http://www.stsci.edu/software/tinytim/tinytim.html

Kundu A., Whitmore B. C., 2001a, AJ, 121, 2950

Kundu A., Whitmore B. C., 2001b, AJ, 122, 1251

Larsen S. S., 1999, A&AS, 139, 393

Larsen S. S., Brodie J. P., Huchra J. P., Forbes D. A., Grillmair C. J., 2001, AJ, 121, 2974

Lee M. G., Freedman W. L., Madore B. F., 1993, ApJ, 417, 553

Lee Y.-W., Gim H. B., Casetti-Dinescu D. I., 2007, ApJL, 661, L49

Liu C., Hu J., Zhao Y., 2006, astro-ph/0612173

Mackey A. D., van den Bergh S., 2005, MNRAS, 360, 631

Martinez-Delgado D., Penarrubia J., Gabany R. J., Trujillo I., Majewski S. R., Pohlen M., 2008, ArXiv e-prints, 805

McLaughlin D. E., Fall S. M., 2008, ApJ, 679, 1272

McLaughlin D. E., van der Marel R. P., 2005, ApJS, 161, 304

Meylan G., Heggie D. C., 1997, A&ARv, 8, 1

Miller B. W., Lotz J. M., 2007, ApJ, 670, 1074

Miller B. W., Lotz J. M., Ferguson H. C., Stiavelli M., Whitmore B. C., 1998, ApJL, 508, L133

Olsen K. A. G., Miller B. W., Suntzeff N. B., Schommer R. A., Bright J., 2004, AJ, 127, 2674

Peng E. W., Jordán A., Côté P., Blakeslee J. P., Ferrarese L., Mei S., West M. J., Merritt D., Milosavljević M., Tonry J. L., 2006, ApJ, 639, 95

Peng E. W., Jordan A., Cote P., Takamiya M., West M. J., Blakeslee J. P., Chen C.-W., Ferrarese L., Mei S., Tonry J. L., West A. A., 2008, astro-ph/0803.0330, 803

Pipino A., Puzia T. H., Matteucci F., 2007, ApJ, 665, 295

Puzia T. H., Kissler-Patig M., Brodie J. P., Huchra J. P., 1999, AJ, 118, 2734

Puzia T. H., Kissler-Patig M., Thomas D., Maraston C., Saglia R. P., Bender R., Richtler T., Goudfrooij P., Hempel M., 2004, A&A, 415, 123

Puzia T. H., Sharina M. E., 2008, ApJ, 674, 909

Puzia T. H., Zepf S. E., Kissler-Patig M., Hilker M., Minniti D., Goudfrooij P., 2002, A&A, 391, 453

Ryan R. E. J., Hathi N. P., Cohen S. H., Malhotra S., Rhoads J., Windhorst R. A., Budavári T., Pirzkal N., Xu C., Panagia N., Moustakas L., di Serego Alighieri S., Yan H., 2007, ApJ, 668, 839

Schlegel D. J., Finkbeiner D. P., Davis M., 1998, ApJ, 500, 525

Schweizer F., 1987, in Faber S. M., ed., Nearly Normal Galaxies. From the Planck Time to the Present Star formation in colliding and merging galaxies. pp 18–25

Schweizer F., 2002, in Geisler D., Grebel E. K., Minniti D., eds, Extragalactic Star Clusters Vol. 207 of IAU Symposium, Evolution of Globular Clusters Formed in Mergers. pp 630–+

Searle L., Zinn R., 1978, ApJ, 225, 357

Seth A., Olsen K., Miller B., Lotz J., Telford R., 2004, AJ, 127, 798

Sharina M. E., Puzia T. H., Makarov D. I., 2005, A&A, 442, 85

Sirianni M., Jee M. J., Benítez N., Blakeslee J. P., Martel A. R., Meurer G., Clampin M., De Marchi G., Ford H. C., Gilliland R., Hartig G. F., Illingworth G. D., Mack J., McCann W. J., 2005, PASP, 117, 1049

Spitler L. R., Larsen S. S., Strader J., Brodie J. P., Forbes D. A., Beasley M. A., 2006, AJ, 132, 1593

Spitzer L., 1987, Dynamical evolution of globular clusters. Princeton, NJ, Princeton University Press, 1987, 191 p.

Spitzer L. J., Thuan T. X., 1972, ApJ, 175, 31

Stiavelli M., Fall S. M., Panagia N., 2004, ApJ, 600, 508

Tully R. B., Rizzi L., Dolphin A. E., Karachentsev I. D., Karachentseva V. E., Makarov D. I., Makarova L., Sakai S., Shaya E. J., 2006, AJ, 132, 729

van den Bergh S., 2000, PASP, 112, 932

Vesperini E., 2000, MNRAS, 318, 841

Whitmore B. C., Schweizer F., 1995, AJ, 109, 960

Zinn R., 1993, in Smith G. H., Brodie J. P., eds, ASP Conf. Ser. 48: The Globular Cluster-Galaxy Connection The Galactic Halo Cluster Systems: Evidence for Accretion. pp 38–+

Table 2. General properties of studied dwarf galaxies.

ID (1)	R.A. (J2000.0) (2)	Decl. (J2000.0) (3)	Morph. Type^a T (4)	(5)	D^b Mpc (6)	$m-M^b$ mag (7)	E_{B-V} mag (8)	M_V mag (9)	$(V-I)_0$ mag (10)	M_{HI} $10^7 M_\odot$ (11)
— Cen A/M83 complex —										
Cen N	13:48:09.2	−47:33:54.0	?	dSph	3.77	27.88	0.079	−11.15	1.24	–
ESO 059-01	07:31:19.3	−68:11:10	10	IB	4.57	28.30	0.147	−14.60	0.78	8.26
ESO 137-18	16:20:59.3	−60:29:15	5.0	SAsc	6.4	29.03	0.243	−17.21	0.79	34.14
ESO 215-09	10:57:30.2	−48:10:44	10	I	5.25	28.60	0.221	−14.08	0.80	64.21
ESO 223-09	15:01:08.5	−48:17:33	9.7	IAB	6.49	29.06	0.260	−16.47	0.88	63.89
ESO 269-58	13:10:32.9	−46:59:27	9.4	I	3.8	27.90	0.106	−15.78	0.98	2.31
ESO 269-66	13:13:09.2	−44:53:24	−5	dE,N	3.82	27.91	0.093	−13.89	1.00	–
ESO 274-01	15:14:13.5	−46:48:45	6.6	Scd	3.09	27.45	0.257	−17.47^a	1.03^a	20.18
ESO 320-14	11:37:53.4	−39:13:14	10	I	6.08	28.92	0.142	−13.67	0.80	2.25
ESO 381-18	12:44:42.7	−35:58:00	9	I	5.32	28.63	0.063	−13.39	0.72	2.71
ESO 381-20	12:46:00.4	−33:50:17	9.8	IBm	5.44	28.68	0.065	−14.80	0.63	15.71
ESO 384-16	13:57:01.6	−35:20:02	−5	dSph/Im	4.53	28.28	0.074	−13.72	0.87	–
ESO 443-09	12:54:53.6	−28:20:27	10	Im	5.97	28.88	0.065	−12.19	0.74	1.44
ESO 444-78	13:36:30.8	−29:14:11	9.9	Im	5.25	28.60	0.053	−13.48	0.86	2.06
HIPASS J1348-37	13:48:33.9	−37:58:03	10	I	5.75	28.78	0.077	−10.80	0.79	0.78
HIPASS J1351-47	13:51:22.0	−47:00:00	10	I	5.73	28.79	0.145	−11.55	0.68	2.69
IC 4247	13:26:44.4	−30:21:45	1.6	Sab	4.97	28.48	0.062	−14.69	0.66	3.45
IKN	10:08:05.9	+68:23:57	−3	dSph	3.75	27.87	0.061	−11.51^c	0.7^c	–
KK 189	13:12:45.0	−41:49:55	−5	dE	4.42	28.23	0.114	−11.99	0.92	–
KK 196	13:21:47.1	−45:03:48	9.8	IBm	3.98	28.00	0.084	−10.72	0.71	–
KK 197	13:22:01.8	−42:32:08	10	Im	3.87	27.94	0.154	−13.04	1.16	0.17
KKS 55	13:22:12.4	−42:43:51	−3	dSph	3.94	27.98	0.146	−11.17	1.22	–
KKS 57	13:41:38.1	+42:34:55	−3	I	3.93	27.97	0.091	−10.73	1.08	–
NGC 5237	13:37:38.9	−42:50:51	1.4	dSph/I	3.4	27.66	0.096	−15.45	0.91	3.10
— Sculptor group —										
ESO 349-31	00:08:13.3	−34:34:42	10	IB	3.21	27.53	0.012	−11.87	0.66	1.34
NGC 247	00:47:06.1	−20:39:04	6.7	SABd	3.65	27.81	0.018	−18.76^a	0.85^a	37.60
— Mafei 1 & 2 —										
KKH 6	01:34:51.6	+52:05:30	10	I	3.73	27.86	0.351	−12.66	0.80	1.34
— IC 342 group —										
KKH 37	06:47:46.9	+80:07:26	10	I	3.39	27.65	0.076	−12.07	0.80	0.48
UGCA 86	03:59:48.3	+67:08:18.6	9.9	Im	2.96	27.36	0.942	−16.13^d	0.80^d	48.25
UGCA 92	04:32:04.9	+63:36:49.0	10	Im	3.01	27.39	0.792	−14.71	0.51	7.62
— NGC 2903 group —										
D 564-08	09:19:30.0	+21:36:11.7	10	I	8.67	29.69	0.029	−12.76	1.00	1.93
D 565-06	09:19:29.4	+21:36:12	10	I	9.08	29.79	0.039	−12.88	0.95	0.54
— CVn I cloud —										
NGC 4068	12:04:02.4	+52:35:19	9.9	Im	4.31	28.17	0.022	−15.25	0.63	11.22
NGC 4163	12:12:08.9	+36:10:10	9.9	Im	2.96	27.36	0.020	−14.21	0.80	1.42
UGC 8215	13:08:03.6	+46:49:41	9.9	Im	4.55	28.29	0.010	−12.51	0.82	1.84
UGC 8638	13:39:19.4	+24:46:33	9.9	Im	4.27	28.15	0.013	−13.69	0.74	1.17
— Field —										
D 634-03	09:08:53.5	+14:34:55	10	I	9.46	29.90	0.038	−11.94	0.92	0.49
DDO 52	08:28:28.5	+41:51:24	10	I	10.28	30.06	0.037	−14.98	0.80	19.99
ESO 121-20	06:15:54.5	−57:43:35	10	I	6.05	28.91	0.040	−13.64	0.68	11.49
HIPASS J1247-77	12:47:32.6	−77:35:01	10	Im	3.16	27.50	0.748	−12.86	0.20	1.05
HS 117	10:21:25.2	+71:06:58	10	I	3.96	27.99	0.115	−11.31	0.91	–
IC 4662	17:47:06.3	−64:38:25	9.7	IBm	2.44	26.94	0.070	−15.58	0.66	12.58
KK 182	13:05:02.9	−40:04:58	10	I	5.78	28.81	0.101	−13.10	0.63	4.45
KK 230	14:07:10.7	+35:03:37	10	I	1.92	26.42	0.014	−9.06	0.74	0.17
KK 246	20:03:57.4	−31:40:54	10	I	7.83	29.47	0.296	−13.77	0.83	11.92
KKH 77	12:14:11.3	+66:04:54	10	I	5.42	28.67	0.019	−14.58^a	0.7^c	4.67
NGC 4605	12:39:59.4	+61:36:33	4.9	SBc	5.47	28.69	0.014	−18.41^a	0.7^c	25.88
UGC 7369	12:19:38.8	+29:52:59	7.6	dE/dE,N?	11.6	30.32	0.019	−16.17	1.03	–
VKN	08:40:08.9	+68:26:23	−3	dSph?	3.4	–	0.035	−10.52^c	0.7^c	–

[a] From LEDA/NED

[b] Distance and distance modulus from Karachentsev et al. (2006, 2007)

[c] Estimated from the total B magnitudes assuming average $B-V=0.45$ and $V-I=0.7$ mag (see Sect.3.1).

Table 3. Globular cluster candidate properties

ID (1)	RA,DEC (2000) [hh:mm:ss],[dd:mm:ss] (2)	M_V [mag] (3)	$(V-I)_0$ [mag] (4)	r_h [pc] (5)	ϵ (6)	$\mathrm{r_{proj}}$ [kpc] (7)	$\mathrm{r_{proj}/r_{eff}}$ (8)
dIrrs							
E115-021-01	02:37:54.24 −61 : 18 : 45.39	−4.79 ± 0.05	1.473 ± 0.052	4.23 ± 0.26	0.18	2.10	1.52
E154-023-01	02:56:49.17 −54 : 33 : 16.51	−4.78 ± 0.06	1.045 ± 0.066	2.27 ± 0.30	0.13	2.01	0.75
E154-023-02	02:57:01.03 −54 : 35 : 24.44	−4.78 ± 0.06	1.129 ± 0.062	1.24 ± 0.25	0.20	3.22	1.09
E154-023-03	02:57:01.06 −54 : 35 : 11.54	−4.40 ± 0.05	1.277 ± 0.053	2.18 ± 0.42	0.14	3.07	1.02
IC1959-01	03:33:20.36 −50 : 23 : 35.17	−5.43 ± 0.05	1.459 ± 0.051	3.57 ± 0.32	0.07	3.15	2.61
IC1959-02	03:33:14.24 −50 : 25 : 40.16	−6.19 ± 0.06	1.028 ± 0.063	6.65 ± 0.36	0.37	1.51	1.42
IC1959-03	03:33:15.70 −50 : 23 : 39.77	−5.42 ± 0.05	1.539 ± 0.051	2.77 ± 0.35	0.42	2.30	1.83
IC1959-04	03:33:12.43 −50 : 24 : 52.60	−9.83 ± 0.05	0.968 ± 0.052	2.92 ± 0.20	0.08	0.03	0.19
IC1959-05	03:33:11.51 −50 : 24 : 38.34	−6.54 ± 0.06	1.096 ± 0.062	1.79 ± 0.23	0.17	0.47	0.22
IC1959-06	03:33:07.70 −50 : 23 : 17.16	−7.60 ± 0.05	0.893 ± 0.052	1.91 ± 0.22	0.08	3.08	2.39
IC1959-07	03:33:15.71 −50 : 25 : 31.32	−6.11 ± 0.06	0.780 ± 0.074	3.77 ± 0.28	0.10	1.48	1.41
IC1959-08	03:33:09.50 −50 : 25 : 45.00	−4.66 ± 0.05	0.990 ± 0.052	1.26 ± 0.25	0.14	1.77	1.56
IC1959-09	03:33:03.47 −50 : 25 : 08.15	−5.07 ± 0.06	1.077 ± 0.070	1.45 ± 0.26	0.42	2.57	2.07
KK16-01	01:55:23.51 +27 : 57 : 29.12	−5.29 ± 0.06	1.034 ± 0.062	2.52 ± 0.30	0.22	1.19	2.49
KK17-01	02:00:15.85 +28 : 50 : 42.59	−4.59 ± 0.05	1.210 ± 0.058	1.19 ± 0.24	0.07	2.11	8.41
KK27-01	03:21:01.00 −66 : 19 : 13.72	−5.24 ± 0.06	1.570 ± 0.067	3.21 ± 0.19	0.16	0.25	0.88
KK27-02	03:20:57.69 −66 : 19 : 03.74	−6.17 ± 0.06	1.183 ± 0.071	3.18 ± 0.19	0.05	0.67	2.61
KK27-03	03:20:50.39 −66 : 19 : 38.16	−4.83 ± 0.05	1.005 ± 0.053	1.43 ± 0.18	0.21	1.61	7.05
KK65-01	07:42:33.50 +16 : 33 : 40.77	−6.12 ± 0.06	1.475 ± 0.070	1.69 ± 0.48	0.40	0.92	0.87
N1311-01	03:20:20.05 −52 : 10 : 14.95	−5.03 ± 0.05	1.089 ± 0.055	2.22 ± 0.29	0.20	3.39	2.95
N1311-02	03:20:17.96 −52 : 11 : 05.37	−5.70 ± 0.05	1.381 ± 0.051	2.03 ± 0.25	0.24	2.57	2.24
N1311-03	03:20:04.05 −52 : 11 : 34.39	−6.48 ± 0.06	1.656 ± 0.064	4.48 ± 0.31	0.23	1.04	0.71
N1311-04	03:20:04.00 −52 : 09 : 21.26	−6.49 ± 0.06	0.819 ± 0.064	8.48 ± 0.21	0.23	2.97	2.52
N1311-05	03:20:07.86 −52 : 11 : 11.03	−8.60 ± 0.05	0.900 ± 0.052	2.09 ± 0.20	0.10	0.12	0.22
N1311-06	03:20:06.69 −52 : 10 : 56.18	−7.33 ± 0.06	0.795 ± 0.067	10.32 ± 0.18	0.07	0.39	0.39
N784-01	02:01:18.09 +28 : 48 : 42.92	−7.54 ± 0.06	0.956 ± 0.062	2.93 ± 0.20	0.15	2.02	0.98
N784-02	02:01:12.29 +28 : 50 : 50.86	−6.10 ± 0.06	1.553 ± 0.064	1.20 ± 0.24	0.29	1.98	0.75
N784-03	02:01:16.42 +28 : 49 : 52.81	−6.65 ± 0.05	0.866 ± 0.056	4.54 ± 0.24	0.12	0.29	0.25
N784-04	02:01:16.57 +28 : 51 : 38.43	−6.40 ± 0.06	0.717 ± 0.076	11.55 ± 0.25	0.09	2.44	0.88
N784-07	02:01:18.31 +28 : 49 : 44.61	−5.72 ± 0.06	1.202 ± 0.074	2.60 ± 0.21	0.10	0.62	0.37
N784-08	02:01:21.32 +28 : 49 : 45.61	−4.39 ± 0.06	1.127 ± 0.078	2.66 ± 0.34	0.37	1.50	0.67
N784-09	02:01:18.54 +28 : 52 : 05.14	−6.62 ± 0.06	0.752 ± 0.070	12.85 ± 0.26	0.08	3.15	1.18
U1281-01	01:49:38.95 +32 : 35 : 09.73	−7.41 ± 0.06	1.240 ± 0.063	6.14 ± 0.32	0.07	2.34	1.53
U1281-02	01:49:32.54 +32 : 35 : 25.26	−7.59 ± 0.05	0.959 ± 0.055	2.01 ± 0.23	0.08	0.38	0.12
U3755-01	07:13:51.95 +10 : 31 : 42.11	−9.20 ± 0.06	0.773 ± 0.062	1.62 ± 0.25	0.27	0.92	0.96
U3755-02	07:13:50.61 +10 : 30 : 40.01	−7.28 ± 0.06	0.986 ± 0.062	2.16 ± 0.28	0.09	1.42	0.85
U3755-03	07:13:50.40 +10 : 31 : 48.33	−6.60 ± 0.07	0.928 ± 0.075	4.31 ± 0.36	0.25	1.27	1.26
U3755-04	07:13:50.12 +10 : 32 : 15.02	−8.75 ± 0.05	1.003 ± 0.051	1.73 ± 0.25	0.08	2.21	1.95
U3755-05	07:13:52.78 +10 : 30 : 42.62	−6.66 ± 0.05	1.038 ± 0.069	6.81 ± 0.46	0.09	1.41	0.71
U3755-06	07:13:52.13 +10 : 31 : 23.98	−8.24 ± 0.06	0.870 ± 0.063	5.97 ± 0.28	0.05	0.40	0.48
U3755-07	07:13:52.06 +10 : 31 : 12.28	−7.35 ± 0.06	0.835 ± 0.067	7.75 ± 0.30	0.16	0.33	0.18
U3755-08	07:13:51.43 +10 : 30 : 57.23	−8.27 ± 0.05	0.885 ± 0.057	6.96 ± 0.32	0.20	0.72	0.29
U3755-09	07:13:50.24 +10 : 31 : 10.73	−6.64 ± 0.06	1.194 ± 0.064	8.54 ± 0.37	0.01	0.72	0.66
U3974-01	07:41:59.49 +16 : 49 : 00.92	−7.21 ± 0.06	0.840 ± 0.063	6.60 ± 0.35	0.16	2.77	0.86
U3974-02	07:41:58.16 +16 : 48 : 16.12	−8.77 ± 0.06	0.959 ± 0.062	2.23 ± 0.29	0.11	1.13	0.44
U3974-03	07:41:58.08 +16 : 47 : 50.52	−7.86 ± 0.05	0.929 ± 0.052	3.34 ± 0.31	0.14	1.23	0.47
U3974-04	07:41:54.87 +16 : 47 : 54.72	−8.28 ± 0.06	0.979 ± 0.075	2.73 ± 0.29	0.09	0.91	0.18

Table 3 (cont'd)

ID (1)	RA,DEC (2000) [hh:mm:ss],[dd:mm:ss] (2)	M_V [mag] (3)	$(V-I)_0$ [mag] (4)	r_h [pc] (5)	ϵ (6)	$\mathrm{r_{proj}}$ [kpc] (7)	$\mathrm{r_{proj}/r_{eff}}$ (8)
U3974-05	07:41:54.57 $+16:48:33.71$	-8.72 ± 0.06	1.321 ± 0.072	10.43 ± 0.27	0.17	1.38	0.30
U4115-01	07:57:03.79 $+14:22:41.01$	-7.62 ± 0.06	0.952 ± 0.062	3.30 ± 0.32	0.08	1.93	0.91
U4115-02	07:56:54.05 $+14:23:40.30$	-5.73 ± 0.05	1.189 ± 0.052	4.20 ± 0.47	0.24	4.28	3.07
U4115-03	07:56:59.20 $+14:21:53.09$	-6.45 ± 0.06	1.221 ± 0.064	4.50 ± 0.39	0.14	3.68	2.28
U4115-04	07:57:01.16 $+14:24:22.25$	-4.95 ± 0.07	1.251 ± 0.089	3.26 ± 0.54	0.36	2.22	1.76
U4115-05	07:57:03.97 $+14:22:26.30$	-4.86 ± 0.06	1.342 ± 0.069	0.52 ± 0.41	0.77	2.45	1.25
U685-01	01:07:26.18 $+16:40:56.84$	-7.02 ± 0.06	0.929 ± 0.062	3.17 ± 0.16	0.00	1.28	1.88
U685-02	01:07:26.77 $+16:40:30.71$	-4.67 ± 0.06	1.730 ± 0.062	1.06 ± 0.21	0.29	1.66	2.39
U685-03	01:07:25.68 $+16:40:44.19$	-7.95 ± 0.06	0.968 ± 0.068	8.53 ± 0.16	0.07	1.20	1.75
U685-04	01:07:23.60 $+16:41:21.88$	-8.64 ± 0.05	0.896 ± 0.052	1.80 ± 0.16	0.12	0.56	0.88
U685-05	01:07:24.64 $+16:40:37.05$	-7.84 ± 0.05	0.954 ± 0.053	4.44 ± 0.18	0.07	1.00	1.40
U685-06	01:07:22.24 $+16:41:15.14$	-8.36 ± 0.05	0.893 ± 0.051	1.66 ± 0.19	0.10	0.22	0.36
U8760-01	13:50:50.73 $+38:01:48.27$	-4.80 ± 0.06	1.275 ± 0.068	5.29 ± 0.22	0.26	0.60	0.89
D565-06-01	09:19:29.66 $+21:36:00.15$	-6.10 ± 0.07	1.583 ± 0.094	1.19 ± 0.41	0.07	0.53	0.72
D634-03-01	09:08:53.72 $+14:34:55.87$	-7.08 ± 0.07	1.039 ± 0.094	5.93 ± 0.46	0.13	0.30	0.08
DDO52-01	08:28:27.09 $+41:51:21.71$	-6.62 ± 0.07	1.004 ± 0.099	3.34 ± 0.42	0.09	0.80	0.43
DDO52-02	08:28:32.70 $+41:52:26.84$	-7.05 ± 0.08	0.958 ± 0.122	6.78 ± 0.47	0.03	3.90	2.04
E059-01-01	07:31:18.26 $-68:11:14.49$	-9.89 ± 0.06	0.907 ± 0.077	2.35 ± 0.15	0.05	0.12	0.01
E121-20-01	06:15:50.13 $-57:43:27.48$	-6.01 ± 0.07	1.335 ± 0.096	2.70 ± 0.26	0.09	1.11	2.56
E223-09-01	15:01:08.38 $-48:16:00.56$	-8.13 ± 0.06	0.992 ± 0.078	4.53 ± 0.23	0.11	2.96	1.00
E223-09-02	15:01:10.40 $-48:16:00.95$	-7.87 ± 0.07	0.982 ± 0.090	3.37 ± 0.23	0.02	3.00	1.01
E223-09-03	15:01:02.81 $-48:17:40.69$	-8.00 ± 0.06	1.019 ± 0.078	4.03 ± 0.25	0.19	1.86	0.65
E223-09-04	15:01:04.59 $-48:17:29.36$	-7.76 ± 0.07	0.853 ± 0.090	5.77 ± 0.28	0.02	1.30	0.46
E223-09-05	15:01:05.91 $-48:17:53.93$	-9.14 ± 0.06	1.072 ± 0.077	3.30 ± 0.23	0.10	1.06	0.38
E223-09-06	15:01:09.85 $-48:17:33.95$	-9.72 ± 0.06	0.921 ± 0.077	3.51 ± 0.25	0.21	0.36	0.11
E223-09-07	15:01:09.75 $-48:18:00.87$	-6.84 ± 0.07	0.952 ± 0.094	2.17 ± 0.23	0.21	0.89	0.32
E223-09-08	15:01:17.37 $-48:17:54.92$	-6.70 ± 0.07	0.915 ± 0.092	2.30 ± 0.28	0.28	2.79	0.95
E269-58-01	13:10:25.66 $-47:00:03.41$	-6.33 ± 0.07	0.773 ± 0.092	5.41 ± 0.33	0.15	1.66	1.16
E269-58-02	13:10:29.41 $-46:58:19.36$	-7.97 ± 0.06	0.820 ± 0.077	2.57 ± 0.14	0.10	1.54	1.17
E269-58-03	13:10:31.20 $-46:59:23.11$	-6.86 ± 0.06	1.127 ± 0.078	14.98 ± 0.13	0.18	0.51	0.32
E269-58-04	13:10:32.08 $-47:00:57.67$	-7.43 ± 0.06	0.923 ± 0.078	2.98 ± 0.17	0.04	1.65	1.20
E269-58-05	13:10:35.55 $-46:58:07.17$	-7.20 ± 0.06	0.918 ± 0.078	4.34 ± 0.13	0.03	1.56	1.25
E269-58-06	13:10:35.88 $-46:59:32.51$	-6.62 ± 0.06	1.104 ± 0.079	18.56 ± 4.04	0.08	0.39	0.39
E269-58-07	13:10:39.50 $-46:59:20.17$	-7.23 ± 0.06	0.944 ± 0.078	2.90 ± 0.15	0.06	1.09	0.93
E269-58-08	13:10:41.34 $-46:59:00.47$	-6.69 ± 0.06	0.941 ± 0.079	7.79 ± 6.04	0.11	1.52	1.26
E320-14-01	11:37:50.70 $-39:12:26.91$	-6.16 ± 0.07	1.471 ± 0.092	3.97 ± 0.29	0.17	1.70	2.89
E349-031-01	00:08:15.16 $-34:36:35.17$	-5.15 ± 0.07	1.293 ± 0.091	0.69 ± 0.12	0.24	1.81	4.21
E349-031-02	00:08:12.64 $-34:36:29.97$	-4.39 ± 0.07	1.229 ± 0.101	6.45 ± 0.18	0.18	1.71	3.99
E381-20-01	12:46:03.21 $-33:49:16.77$	-5.39 ± 0.07	1.344 ± 0.098	4.13 ± 0.18	0.15	1.78	1.87
E384-016-01	13:56:54.28 $-35:18:26.01$	-5.93 ± 0.07	1.160 ± 0.090	2.14 ± 0.15	0.22	2.84	4.54
E384-016-02	13:56:59.90 $-35:19:37.17$	-5.29 ± 0.07	1.271 ± 0.094	1.41 ± 0.17	0.17	0.67	1.01
KK197-01	13:21:59.81 $-42:32:06.51$	-5.69 ± 0.07	1.050 ± 0.094	1.95 ± 0.17	0.01	0.46	1.68
KK197-02	13:22:02.04 $-42:32:08.14$	-9.83 ± 0.06	0.932 ± 0.077	2.95 ± 0.13	0.11	0.00	0.00
KK197-03	13:22:02.53 $-42:32:13.82$	-7.26 ± 0.06	0.925 ± 0.078	2.56 ± 0.17	0.07	0.15	0.53
KK246-01	20:03:57.47 $-31:40:55.93$	-6.72 ± 0.07	0.864 ± 0.098	4.46 ± 0.38	0.18	0.19	0.34
KK246-02	20:03:57.07 $-31:40:58.93$	-8.30 ± 0.06	0.960 ± 0.078	4.24 ± 0.26	0.06	0.16	0.42
KKH77-01	12:14:08.52 $+66:05:41.69$	-7.98 ± 0.06	0.996 ± 0.077	1.97 ± 0.23	0.14	0.00	0.00
KKH77-02	12:14:22.72 $+66:05:38.58$	-5.41 ± 0.07	1.074 ± 0.100	1.77 ± 0.25	0.11	2.27	3.01
KKH77-03	12:14:18.83 $+66:04:27.69$	-5.48 ± 0.07	1.598 ± 0.096	4.76 ± 0.18	0.19	2.55	3.39
N4163-01	12:12:09.70 $+36:10:15.15$	-9.38 ± 0.06	0.915 ± 0.077	1.45 ± 0.10	0.09	0.17	0.27

Table 3 (cont'd)

ID (1)	RA,DEC (2000) [hh:mm:ss],[dd:mm:ss] (2)	M_V [mag] (3)	$(V-I)_0$ [mag] (4)	r_h [pc] (5)	ϵ (6)	$\mathrm{r_{proj}}$ [kpc] (7)	$\mathrm{r_{proj}/r_{eff}}$ (8)
N4163-02	12:12:08.57 +36 : 10 : 25.95	-7.83 ± 0.06	0.969 ± 0.077	2.08 ± 0.10	0.03	0.31	0.53
N5237-01	13:37:37.87 −42 : 51 : 20.02	-8.46 ± 0.06	0.925 ± 0.077	0.68 ± 0.16	0.39	0.55	0.57
N5237-02	13:37:37.95 −42 : 50 : 23.32	-6.85 ± 0.06	0.997 ± 0.078	15.09 ± 0.18	0.12	0.46	0.51
N5237-03	13:37:34.62 −42 : 50 : 01.90	-6.42 ± 0.06	1.131 ± 0.078	3.38 ± 0.11	0.06	1.11	1.20
U8638-01	13:39:26.80 +24 : 45 : 50.46	-6.57 ± 0.06	0.871 ± 0.078	13.63 ± 0.88	0.00	2.26	4.71
U8638-02	13:39:24.83 +24 : 46 : 14.04	-7.72 ± 0.06	0.966 ± 0.077	3.23 ± 0.17	0.05	1.58	3.25
U8638-03	13:39:18.17 +24 : 46 : 18.89	-10.35 ± 0.06	1.077 ± 0.077	2.62 ± 0.14	0.04	0.42	1.02
UA86-04	03:59:38.20 +67 : 07 : 12.70	-6.95 ± 0.07	0.911 ± 0.092	3.19 ± 0.20	0.00	1.42	5.51
UA86-05	03:59:51.07 +67 : 06 : 10.21	-7.53 ± 0.07	0.878 ± 0.089	2.19 ± 0.11	0.06	2.02	8.12
UA86-07	03:59:45.84 +67 : 07 : 07.54	-7.26 ± 0.07	0.738 ± 0.091	1.21 ± 0.16	0.13	1.21	4.57
UA86-10	03:59:49.83 +67 : 06 : 49.71	-11.03 ± 0.06	0.716 ± 0.077	1.14 ± 0.10	0.06	1.45	5.64
UA86-11	03:59:43.02 +67 : 07 : 27.78	-6.80 ± 0.07	1.523 ± 0.089	3.43 ± 0.14	0.30	1.02	3.73
UA86-17	03:59:48.76 +67 : 08 : 16.72	-9.67 ± 0.06	0.731 ± 0.077	3.27 ± 0.13	0.08	0.19	0.30
UA86-20	03:59:42.40 +67 : 08 : 53.83	-7.58 ± 0.07	0.731 ± 0.089	10.78 ± 0.14	0.19	0.63	2.95
UA86-25	03:59:48.88 +67 : 08 : 30.85	-7.99 ± 0.06	0.720 ± 0.078	4.24 ± 0.10	0.03	0.01	0.72
UA86-27	04:00:00.75 +67 : 07 : 37.21	-8.29 ± 0.07	0.703 ± 0.088	7.02 ± 0.18	0.15	1.26	5.28
UA86-28	03:59:49.23 +67 : 08 : 40.76	-7.79 ± 0.07	0.868 ± 0.088	3.11 ± 0.15	0.02	0.16	1.35
UA86-29	03:59:50.29 +67 : 08 : 38.16	-11.16 ± 0.06	1.020 ± 0.077	4.73 ± 0.14	0.12	0.17	1.37
UA86-30	03:59:53.87 +67 : 08 : 30.97	-7.84 ± 0.07	0.769 ± 0.088	4.76 ± 0.24	0.23	0.43	2.18
UA92-02	04:32:03.24 +63 : 37 : 06.65	-8.04 ± 0.06	1.038 ± 0.077	3.13 ± 0.17	0.07	0.28	0.65
UA92-03	04:32:01.94 +63 : 36 : 41.92	-7.74 ± 0.06	0.784 ± 0.078	6.20 ± 0.12	0.15	0.23	0.66
dSphs							
IKN-01	10:08:07.14 +68 : 23 : 36.65	-6.65 ± 0.06	0.911 ± 0.079	6.62 ± 0.29	0.13	0.40	–
IKN-02	10:08:10.79 +68 : 24 : 05.60	-7.15 ± 0.06	0.994 ± 0.078	3.55 ± 0.13	0.14	0.50	–
IKN-03	10:08:05.26 +68 : 24 : 33.78	-6.76 ± 0.07	1.085 ± 0.092	14.81 ± 0.83	0.13	0.66	–
IKN-04	10:08:04.80 +68 : 24 : 53.71	-7.41 ± 0.06	0.936 ± 0.077	1.96 ± 0.16	0.18	1.03	–
IKN-05	10:08:05.52 +68 : 24 : 57.99	-8.47 ± 0.06	0.906 ± 0.077	2.89 ± 0.13	0.12	1.10	–
KKS55-01	13:22:12.41 −42 : 45 : 11.76	-7.36 ± 0.06	0.907 ± 0.078	4.51 ± 0.18	0.11	1.48	4.75
dEs							
E269-66-01	13:13:10.30 −44 : 53 : 00.96	-8.08 ± 0.06	0.911 ± 0.078	2.87 ± 0.15	0.10	0.49	0.81
E269-66-03	13:13:08.84 −44 : 53 : 22.59	-9.99 ± 0.06	0.926 ± 0.077	2.50 ± 0.13	0.13	0.00	0.00
E269-66-04	13:13:03.12 −44 : 53 : 40.16	-7.18 ± 0.06	1.017 ± 0.078	7.48 ± 0.13	0.10	1.17	1.92
E269-66-05	13:13:11.79 −44 : 53 : 09.79	-7.18 ± 0.06	0.873 ± 0.078	4.77 ± 0.19	0.16	0.63	1.03
U7369-01	12:19:40.78 +29 : 52 : 04.71	-6.90 ± 0.07	0.899 ± 0.099	2.77 ± 0.47	0.17	3.43	2.39
U7369-02	12:19:41.50 +29 : 52 : 45.68	-5.83 ± 0.09	0.846 ± 0.156	2.89 ± 0.53	0.07	2.18	1.53
U7369-03	12:19:39.93 +29 : 52 : 37.20	-7.03 ± 0.07	1.027 ± 0.102	2.91 ± 0.42	0.03	1.54	1.07
U7369-04	12:19:37.86 +29 : 52 : 06.76	-5.75 ± 0.09	0.956 ± 0.151	6.59 ± 0.73	0.19	3.03	2.11
U7369-05	12:19:37.32 +29 : 52 : 08.36	-4.95 ± 0.10	1.284 ± 0.162	2.87 ± 0.64	0.18	3.04	2.12
U7369-06	12:19:39.91 +29 : 52 : 52.40	-6.65 ± 0.07	0.996 ± 0.096	3.16 ± 0.53	0.08	0.97	0.68
U7369-09	12:19:38.94 +29 : 53 : 00.92	-6.62 ± 0.07	1.305 ± 0.098	3.42 ± 0.39	0.41	0.19	0.14
U7369-10	12:19:38.70 +29 : 52 : 59.48	-12.08 ± 0.06	0.824 ± 0.077	2.31 ± 0.39	0.16	0.00	0.01
U7369-11	12:19:38.88 +29 : 53 : 05.55	-6.11 ± 0.08	0.901 ± 0.129	2.23 ± 0.56	0.28	0.37	0.26
U7369-12	12:19:39.01 +29 : 53 : 08.45	-5.89 ± 0.08	1.152 ± 0.128	0.55 ± 0.39	0.29	0.55	0.39
U7369-13	12:19:40.37 +29 : 53 : 29.93	-6.84 ± 0.07	0.895 ± 0.101	1.56 ± 0.42	0.18	2.10	1.47
U7369-14	12:19:37.83 +29 : 52 : 57.41	-6.46 ± 0.08	1.069 ± 0.114	3.48 ± 0.50	0.20	0.65	0.45
U7369-15	12:19:37.45 +29 : 52 : 52.53	-7.43 ± 0.07	0.929 ± 0.093	1.13 ± 0.47	0.05	0.99	0.69

Table 3 (cont'd)

ID (1)	RA,DEC (2000) [hh:mm:ss],[dd:mm:ss] (2)	M_V [mag] (3)	$(V-I)_0$ [mag] (4)	$r_{\rm h}$ [pc] (5)	ϵ (6)	$\rm r_{proj}$ [kpc] (7)	$\rm r_{proj}/r_{eff}$ (8)
U7369-16	12:19:38.51 +29 : 53 : 09.36	-5.66 ± 0.09	1.204 ± 0.146	2.29 ± 0.56	0.16	0.57	0.40
U7369-17	12:19:37.81 +29 : 53 : 00.54	-8.22 ± 0.06	0.895 ± 0.079	1.33 ± 0.39	0.05	0.65	0.45
U7369-18	12:19:36.97 +29 : 52 : 58.99	-7.05 ± 0.07	1.081 ± 0.095	1.14 ± 0.39	0.04	1.27	0.88
U7369-19	12:19:38.27 +29 : 53 : 26.03	-7.68 ± 0.07	0.917 ± 0.094	1.86 ± 0.42	0.15	1.52	1.07
U7369-20	12:19:39.43 +29 : 53 : 46.89	-6.27 ± 0.08	1.007 ± 0.121	1.31 ± 0.42	0.17	2.72	1.90
U7369-21	12:19:37.42 +29 : 53 : 16.35	-7.18 ± 0.07	0.910 ± 0.096	1.34 ± 0.42	0.13	1.33	0.93
U7369-22	12:19:37.68 +29 : 53 : 27.93	-6.46 ± 0.08	0.940 ± 0.117	1.54 ± 0.44	0.13	1.77	1.23
U7369-23	12:19:36.34 +29 : 53 : 12.58	-6.68 ± 0.07	0.848 ± 0.104	1.35 ± 0.42	0.20	1.88	1.31
Sms							
E137-18-01	16:20:56.66 −60 : 29 : 08.15	-7.79 ± 0.06	1.030 ± 0.078	3.42 ± 0.21	0.18	0.65	0.31
E137-18-02	16:21:05.09 −60 : 27 : 50.06	-8.16 ± 0.06	0.772 ± 0.079	3.20 ± 0.23	0.10	2.96	1.40
E137-18-03	16:21:00.44 −60 : 29 : 10.65	-7.15 ± 0.07	1.143 ± 0.090	3.11 ± 0.21	0.18	0.29	0.14
E137-18-04	16:21:00.42 −60 : 29 : 43.48	-7.78 ± 0.06	0.900 ± 0.078	3.97 ± 0.23	0.04	0.91	0.43
E137-18-05	16:21:02.92 −60 : 29 : 14.23	-6.99 ± 0.07	0.835 ± 0.092	5.59 ± 0.49	0.05	0.82	0.39
E137-18-06	16:21:00.98 −60 : 30 : 04.40	-6.98 ± 0.07	0.929 ± 0.095	8.10 ± 0.35	0.00	1.57	0.74
E137-18-07	16:21:11.03 −60 : 28 : 37.99	-6.90 ± 0.07	1.339 ± 0.092	5.77 ± 1.30	0.14	2.92	1.39
E274-01-01	15:14:15.65 −46 : 47 : 31.48	-8.56 ± 0.06	1.004 ± 0.077	0.45 ± 0.10	0.41	0.73	0.39
E274-01-02	15:14:12.16 −46 : 48 : 39.53	-7.78 ± 0.06	0.864 ± 0.077	3.97 ± 0.17	0.04	0.48	0.26
E274-01-03	15:14:15.32 −46 : 48 : 09.76	-7.88 ± 0.06	1.093 ± 0.077	2.15 ± 0.10	0.09	0.18	0.10
E274-01-04	15:14:16.49 −46 : 48 : 17.19	-7.16 ± 0.06	1.055 ± 0.078	3.37 ± 0.10	0.09	0.30	0.16
E274-01-06	15:14:19.07 −46 : 48 : 00.91	-7.26 ± 0.06	1.051 ± 0.077	4.92 ± 0.12	0.11	0.75	0.40
E274-01-07	15:14:18.54 −46 : 48 : 24.34	-6.86 ± 0.06	0.945 ± 0.078	2.80 ± 0.10	0.11	0.63	0.33
N247-01	00:47:09.72 −20 : 37 : 40.25	-7.42 ± 0.06	0.859 ± 0.078	16.02 ± 0.28	0.05	1.75	0.31
N247-02	00:47:11.59 −20 : 38 : 48.58	-6.59 ± 0.06	1.138 ± 0.080	18.79 ± 1.01	0.27	1.40	0.25
N4605-01	12:40:11.35 +61 : 34 : 47.80	-5.69 ± 0.07	1.491 ± 0.090	1.49 ± 0.18	0.24	3.60	1.32
N4605-02	12:40:05.08 +61 : 35 : 40.51	-5.51 ± 0.07	0.934 ± 0.101	7.63 ± 0.40	0.10	1.76	0.65
N4605-03	12:40:10.75 +61 : 34 : 57.46	-7.14 ± 0.06	0.974 ± 0.079	9.64 ± 0.40	0.03	3.33	1.22
N4605-04	12:40:06.32 +61 : 35 : 40.27	-8.20 ± 0.06	1.000 ± 0.077	4.12 ± 0.20	0.18	1.92	0.70
N4605-05	12:40:07.61 +61 : 35 : 35.99	-6.77 ± 0.06	1.227 ± 0.079	7.13 ± 0.21	0.14	2.17	0.80
N4605-06	12:40:09.02 +61 : 35 : 26.86	-7.13 ± 0.06	1.036 ± 0.079	2.39 ± 0.22	0.00	2.53	0.93
N4605-08	12:40:13.58 +61 : 35 : 12.72	-6.34 ± 0.07	0.979 ± 0.091	13.63 ± 0.29	0.16	3.43	1.26
N4605-09	12:40:19.99 +61 : 34 : 24.90	-6.01 ± 0.07	0.949 ± 0.098	8.55 ± 0.18	0.14	5.17	1.90
N4605-10	12:40:12.23 +61 : 35 : 30.83	-8.26 ± 0.06	0.969 ± 0.077	19.16 ± 0.25	0.04	2.94	1.08
N4605-11	12:40:16.35 +61 : 35 : 28.57	-7.00 ± 0.06	0.688 ± 0.080	2.72 ± 0.22	0.13	3.64	1.33
N4605-12	12:40:18.42 +61 : 35 : 37.99	-5.41 ± 0.08	1.240 ± 0.113	2.55 ± 0.25	0.16	3.89	1.43

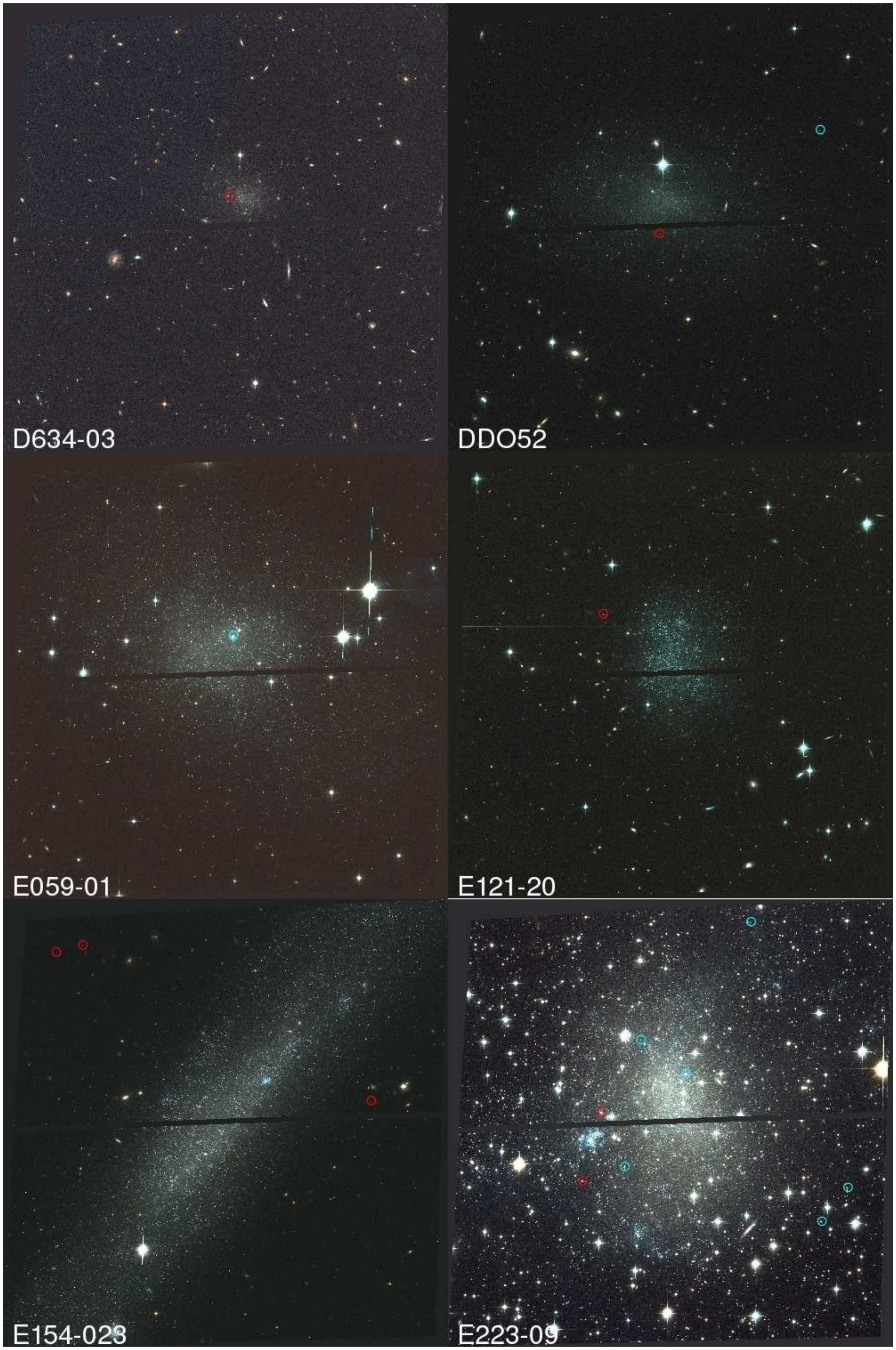

Figure 9. HST/ACS color composite images of the dwarf galaxies presented in this study. With blue, red and magenta circles are shown the blue and red GC candidates and likely background contaminants, respectively. For the blue green and red channels we used $V, (V + I)/2$ and $I-$band HST/ACS images. (The full version of this figure is available upon request).